The Hebrew University of Jerusalem
Faculty of Mathematics and Sciences
Selim and Rachel Benin School of Engineering
Applied Physics Department

Nonlinear Optical Waveguides from Dilute Composites Consisting of Polymer with Partially Aligned Nanorods

מוליכי-גלים אופטיים לא-ליניאריים מתערובות דלילות המכילות פולימר וננו-מוטות בעלי כיווניות חלקית

by

Yedidya Lior

This work was done under the supervision of

Dr. Dan M. Marom

Thesis submitted for M.Sc. degree

December, 2012

Acknowledgments

I first wish to thank my wife Roni for her support, encouragement and patience. I thank her for many days and nights alone, when I was working on this research. Without her, this work was not possible.

I thank my father in law, Assaf, for the endless brainstorming.

I thank my advisor Dr. Dan Marom for his guidance and for giving me the platform for this research. His guidance and advices enabled me to reach the finishing line of this work.

Finally, I wish to thank Prof. Ari Sihvola from the School of Electrical Engineering at the Aalto University, Finland and Prof. Alexander Shik from the Center for Advanced Nanotechnology at the University of Toronto, Canada. Both of them helped me understanding their work and helped me with my ideas, without even knowing me.

Abstract

The expected permittivity and third order nonlinear susceptibility, of a low filling fraction composite consisting of semiconductor nanorods dispersed in a polymer host are derived, using the Maxwell-Garnett model for anisotropic nonlinear inclusions. The semiconductor nanorods are modeled both as prolate spheroids and more realistic capsule shapes. A new generalized model is presented for various nanorod axis orientation statistics, achieved by an aligning electric field. The angular distribution function of the nanorods is calculated for nanorods with a permanent electrical dipole moment, which assists the alignment of the nanorods. Using the angular distribution function, the composite macroscopic characteristics are found for a composite with random orientation, partially aligned and nematic array nanorods. As the alignment field strength increases, the composite optical properties asymptotically converge towards the nematic case. Different parameters relate to the nanorods geometry are examined, concluding that the main parameter influencing the alignment is the single NR volume, while for the nematic array the single nanorod axes aspect-ration is the major parameter. Due to the symmetry of the nanorods, the composite characteristics depend on the polarization of the optical electrical field, with a symmetry that resembles a uniaxial crystal.

A nonlinear waveguide with a core made of such a composite is simulated, in order to find the nonlinear parameter of the waveguide. The model takes into account two electrodes for the alignment process, far enough from the waveguide core, in order to avoid losses to the optical mode. Significant optical response can be achieved even for randomly oriented nanorods composite, with a nonlinear parameter of $68(W\times m)^{-1}$. The alignment process increases the nonlinear parameter significantly even at elevated temperature that are needed for polymerization of the polymer host, typically $150^{o}C$. Aligning field strength of 10^{7} V/m results with very high value for the nonlinear parameter – $120(W\times m)^{-1}$, much higher than ordinary glass based nonlinear optical fibers, that result with nonlinear parameter up to $50(W\times m)^{-1}$.

תקציר

הערכים של המקדם הדיאלקטרי וההיענות החשמלית הלא-ליניארית מסדר שלישי, מחושבים עבור תערובת המכילה ננו-מוטות מחומר מוליך למחצה, המפוזרים בפולימר בשבר נפחי נמוך, על-ידי הרחבה של מודל מקסוול-גרנט, לגופים אנאיזוטרופיים ולא-ליניאריים. הננו-מוטות מיוצגים במודל כספירואיד אובלי ובמודל מציאותי יותר כצורת כמוסה. מודל מורחב חדש מוצג עבור סטטיסטיקות שונות של כיווניות הננו-מוטות, המושגות באמצעות שדה חשמלי מכוון. פונקצית ההתפלגות הזוויתית של הננו-מוטות מחושבת עבור ננו-מוטות עם מומנט דיפול חשמלי קבוע, אשר מסייע להתכווננות של הננו-מוטות. על-ידי פונקצית ההתפלגות הזוויתית, המאפיינים המקרוסקופיים של התערובת מחושבים עבור רמות שונות של כיווניות של הננו-מוטות – כיווניות רנדומלית, כיווניות חלקית וכיווניות מלאה (מערך נמטי). ככל שעצמת השדה המכוון גדלה, המאפיינים האופטיים של התערובת מתכנסים בצורה אסימפטוטית, לעבר הערך של המערך הנמטי. פרמטרים שונים ביחס לגיאומטריה של הננו-מוטות נבחנים, כאשר המסקנה היא שהפרמטר העיקרי המשפיע על הכיווניות הוא הנפח של הננו-מוט הבודד, בעוד שעבור המערך הנמטי הפרמטר העיקרי הוא יחס הצירים של הננו-מוט הבודד. כתוצאה מהסימטריה של הננו-מוטות, המאפיינים של התערובת תלויים בקיטוב של השדה החשמלי האופטי, עם סימטריה הדומה לזו של גביש חד-צירי.

מוליך גל לא-ליניארי בעל ליבה העשויה מהתערובת ממודל, על-מנת לחשב את הפרמטר הלא-ליניארי של מוליך הגל. המודל לוקח בחשבון שתי אלקטרודות עבור תהליך הכוונון, הרחוקות מספיק מליבת מוליך-הגל, כדי להימנע מהפסדים במוד האופטי. ניתן להשיג תגובה אופטית משמעותית גם עבור תערובת המכילה ננו-מוטות המכוונים באופן אקראי, כאשר הפרמטר הלא-ליניארי מגיע ל-68(וואט×מטר)$^{-1}$. תהליך הכוונון מגדיל את הגורם הלא-ליניארי בצורה משמעותית, אפילו עבור טמפרטורות גבוהות הנדרשות לפלמור של הפולימר המשמש כסביבה של הננו-מוטות, המתרחש בטמפרטורות של 150^{o}C. עבור עצמת שדה מכוון של 10^{7} וולט למטר, הערך של הפרמטר הלא ליניארי המתקבל הוא 120(וואט×מטר)$^{-1}$, תוצאה גבוהה במיוחד ביחס לסיבים אופטיים לא-ליניאריים רגילים המבוססים על זכוכית, בעלי פרמטר לא ליניארי של עד 50(וואט×מטר)$^{-1}$.

Table of content:

1. Introduction

Nonlinear (NL) optical waveguides (WGs) are an important building block for various optical applications, such as optical switching, phase modulation and wave mixing. Finding the suitable NL material, for a desired application, has an important role in designing the NL WG. Different NL materials are suitable for different needs, when the specific purpose of the WG, the optical wavelength in question and other properties can affect the selection of the NL material. Of course, not every material that has the suitable NL properties for our need has also the suitable properties for being a WG, when considering both fabrication processes and optical properties as low loss etc. An elegant way to combine a suitable NL material into a WG is to use nano-particles (NP) from a NL material inside a host from a material that is proven suitable for optical WGs. The requirements from such a composite of materials is that the NPs will be much smaller that the wavelength in question and homogeneously dispersed in the host.

The physical characteristics of the NPs can be significantly manipulated by controlling their shape to match specific needs. Rod shaped nanocrystals exhibit enhanced optical response along their long axis due to surface polarization [1,2]. Composites consisting of such nanorods (NRs) embedded in a dielectric host, can serve as building block for various optical applications.

Former work by Prof. Banin *et al.* showed an optical WG for wavelength of 1.55μm, constructed from sphere NP inclusions, embedded in a PFCB polymer [3,4]. PFCB (Per-Flourinated Cyclo-Butane) is a good material for use in 1.55μm wavelength, with low losses and tunable refractive index, by synthesis control. The PFCB's low polymerization temperature and thermal stability make it a good candidate as a host for NPs. They showed that for the right capping ligands for the NPs, the optical properties of the NPs are maintained. Elsewhere [5], TiO2 NRs inside PMMA were shown to be a good candidate for NL optical composite media, hence the combination of PFCB with NRs is a very interesting composite to examine for NL WGs. Enhancing the inclusion response by using aligned NRs is the next natural step.

The properties of such a composite will depend on the material and dimensions of the NRs on one hand and on the statistical directionality of the NRs in the composite, on the other hand. Quantitative models that analyze composites with embedded NRs, are mostly based on describing NRs as prolate spheroids in a perfect nematic array (Fig. 1.a), where no statistical measure of the NR alignment spread in the composite is discussed [6,7,8,9]. The configuration of a nematic array can be fabricated in planar (2D) arrays by e-beam lithography [10] or nanosphere lithography [11]. In a volumetric (3D) array achieving the control over the directionality is problematic and thus it is much harder to fabricate perfect 3D nematic array. The natural phase of a composite with dilute NRs dispersed in it is that of randomly oriented NRs. The case of random orientation (Fig. 1.b) was also addressed and compared to the nematic case for the linear material properties [7,8,9]. The case of statistical orientation (Fig. 1.c) was addressed theoretically for the linear regime with an arbitrary distribution function, without analysis and calculations of the origin of the alignment or the statistical behavior influence on the resulting macroscopic characteristics [7,9]. For the statistical case, qualitative description of composites' macroscopic characteristics was made, in terms of the volume the NRs occupy in the composite, rather than the whole composite characteristics [12].

In this work, I present a comprehensive quantitative statistical model for calculating the macroscopic characteristics of such composites, finding their permittivity and third order NL susceptibility. The model takes into account several factors that were ignored previously: the geometry of a single NR is described as a capsule, which better matches most NRs TEM images, the statistical behavior of the NR alignment in the composite, and cases with and without a permanent electrical dipole moment in the NRs.

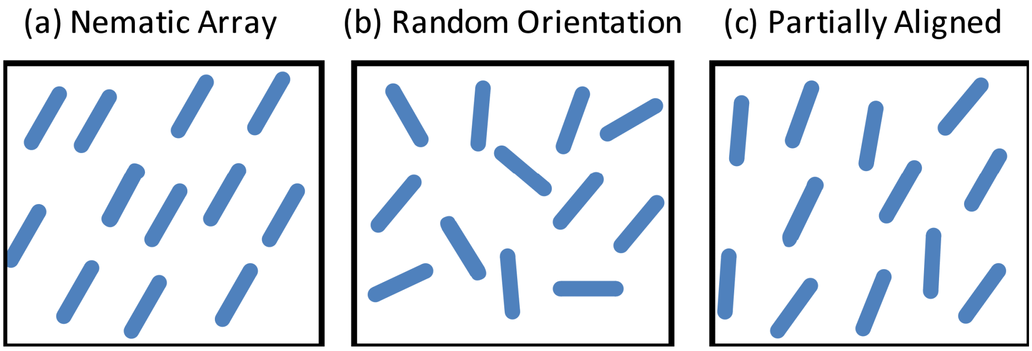

Fig 1. An illustration describing different NRs alignment degree: (a) A perfect nematic array of NRs. (b) Random distributed NRs. (c) An array of partially aligned NRs.

After characterizing the composite, I simulate its properties within a NL WG, with a PFCB-NRs composite core and Cytop cladding. The PFCB core – Cytop cladding WG structure was already fabricated and tested in the Photonics Devices Laboratory (e.g. [13,14]) and the use of the PFCB-NRs mixture is the next step in the lab's research plan.

I will start from describing the physics of a single particle inclusion and its relevant electrostatic and electrodynamic characteristics. I will continue with describing the NRs as capsule shapes instead of the usual description of prolate spheroid and examine the influence of such a description on the electrostatic and electrodynamic characteristics. I will then describe the alignment mechanisms; applied external field and permanent dipole moment in the NRs. I will explain how to use the statistical behavior of the orientation of the NRs, to calculate the macroscopic characteristics of the composite: the permittivity and third order NL susceptibility. I will examine the influence of different parameters on the composite characteristics, focusing on the third order NL susceptibility. I will finish with simulations of a NL WG with such a composite as the core of the WG.

2. Theoretical Background

Some notations are required before diving into the theoretical background. I will use SI unit system and will use the notation $\vec{D}=\varepsilon_0\varepsilon_r\vec{E}$ for the displacement field. Because some of the authors derived their formulas using the Gaussian unit system and some using the SI unit system, there is often a need for converting between the unit systems. In order to clarify comparison and integration of different sources, I chose to write explicitly the vacuum permittivity ε_0. In places I will use Gaussian unit system I will mention it explicitly and use the expression $1/4\pi$ without reducing it. At last, in places I will use relative permittivity of different materials, I will denote that explicitly as well. Regarding NL WGs, I will introduce some important concepts in the opening of the relevant section (section 7), without deeply describing all the theoretical background of this subject.

2.1 Small particles under electric field

2.1.1 Dipole moment, polarizability and depolarization factor

When an electric field $\vec{E}_{ext}$ is applied on a small dielectric particle inside a dielectric surrounding with different permittivity, the field near the particle is perturbed by the particle. Inside the particle, the applied field induces a dipole moment $\vec{\mu}$. In the linear regime of discussion, the dipole moment is given by the formula $\vec{\mu}=\vec{\alpha}\cdot\vec{E}_{ext}$, where α is called the polarizability of the inclusion [7]. In the general case, α is a second rank tensor, which can be represented as a [3×3] matrix. In order to find this induced dipole moment in the inclusion one must start from the internal field inside it, derive the polarization density field and then integrating the polarization density over the volume, find the dipole moment [15]:

$$\vec{\mu}=\int_V \vec{P}\cdot dV \tag{2.1}$$

For the polarizability of an ellipsoid, there are two slightly differing solutions, one presented by Landau & Lifshitz [15] and the other by Sihvola [7]. In Appendix A, I show the differences between the two derivations, and simulation results. As shown in the appendix, the formula presented by Sihvola match my simulations, therefore I will use it. According to Sihvola, the polarizability of an ellipsoid is:

$$\alpha_{Sihvola}^{j} = V\varepsilon_0 \frac{(\varepsilon_i - \varepsilon_h)}{\varepsilon_h + L^j(\varepsilon_i - \varepsilon_h)}\varepsilon_h \qquad (2.2)$$

where $\varepsilon_h, \varepsilon_i$ are the permittivities of the host and ellipsoid inclusion, respectively, V is the ellipsoid volume and L^j is the "depolarization factor" of the ellipsoid in the $j = x, y, z$ directions, which are the major axes of the ellipsoid. The depolarization factor is a geometric factor that expresses the different electrostatic response of the ellipsoid under an electric field, along the ellipsoid different axes. For the prolate spheroid shape (meaning an ellipsoid with two equal short axes (SAs) and one long axis (LA)), I define the $\hat{z}$ axis as the LA, such that $a_z > a_x = a_y$.The depolarization factor for a prolate spheroid is given by [7,15]:

$$L^z = L^{LA} = \frac{1-e^2}{e^2}\left(\frac{1}{2e}\ln\left(\frac{1+e}{1-e}\right) - 1\right) \quad , \quad L^x = L^y = L^{SA} = \frac{1-L^{LA}}{2} \qquad (2.3)$$

where $e = \sqrt{1 - a_x^2/a_z^2}$ is the eccentricity of the prolate spheroid. I refer the derivation of the depolarization factor to Appendix A as well. The three depolarization factors satisfy $L^x + L^y + L^z = 1$. The LA depolarization factor varies between 0 (needle) to 1/3 (sphere) and consequently, the SA depolarization factor varies between 1/2 to 1/3. Larger depolarization factor can be achieved only for an oblate spheroid (two equal LAs and one SA). A prolate spheroid with large aspect ratio (AR=LA/SA) between the LA and the SA, will have a smaller depolarization factor, in the LA direction.

The derivations leading to Eq. (2.2) assume an isotropic material, and the anisotropy of the polarizability is due to the anisotropy of the prolate spheroid shape alone (in contrast to a sphere where the inclusions and the composite remain isotropic).

2.1.2 Rotating moment on a tilted spheroid

The derivation of the polarizability (section 2.1.1 and Appendix A), assumed a spheroid with a major axis parallel to the external electric field. In cases where the spheroid is not parallel to the electric field, the dipole moment $\vec{\mu}$ will not be in any specific known direction. In the general case, the direction of the spheroid should be presented with two angles: (1) The angle θ between the LA of the spheroid and the $\hat{z}$ axis, is the tilt angle which is defined over the interval $\theta = [0, \pi]$. (2) The angle φ between the projection of the LA of the spheroid on the $\hat{x}-\hat{y}$ plane and the $\hat{x}$ axis, is the azimuthal angle which is defined over the interval $\varphi = [0, 2\pi]$ (see Fig. 2.a).

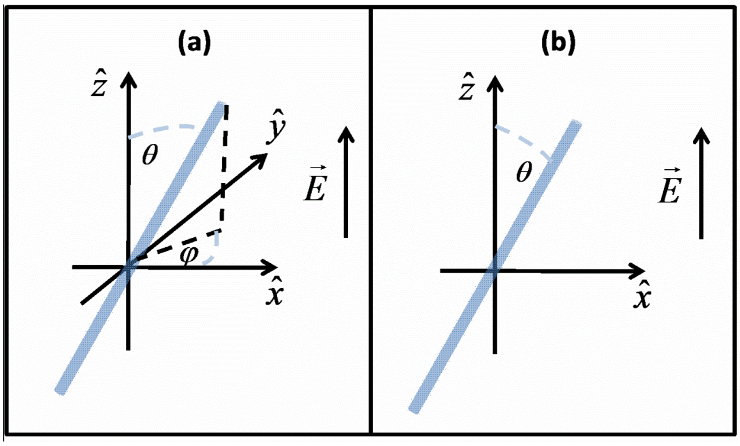

Fig 2. An illustration describing the direction of the prolate spheroid (in blue) in the axes of the system. (a) The general case with 3D presentation and two angles θ and φ. (b) Reduction of the problem to 2D for analysis of the tilt angle θ.

In a shape symmetric to rotation (e.g. spheroids), the interaction is defined in plane containing the vectors of the aligning field and the axis of symmetry of the shape (the LA in our case) [15]. Both the vector of the dipole moment and of the aligning field will be in that plane. Without any lost of generality, I will set the direction of the external electric field as $\hat{z}$ and the dipole moment vector is in the $\hat{y}-\hat{z}$ plane with an angle θ regarding the $\hat{z}$ axis, as illustrated in Fig. 2.b.

The induced dipole moment will have a component in the LA direction – $\mu_{\parallel} = \alpha_{\parallel} E \cos\theta$ and a component in the SA direction – $\mu_{\perp} = \alpha_{\perp} E \sin\theta$ (Fig. 3.a). The interaction between the dipole moment and the original external field will cause a rotating moment $\vec{M}$ on the ellipsoid (Fig. 3.b), which will be [12,15]:

$$\vec{M} = \vec{\mu} \times \vec{E}_{ext} \tag{2.4}$$

Each dipole moment interacts with the field component in the opposite direction (LA and SA direction dipole moments with the SA and LA electric field component, respectively) and cause a rotating moment in an opposite direction. However, for dielectric or semiconductor NRs, the sum of the two rotating moments is always positive, meaning the NR will be align eventually parallel to the external field, as illustrated at Fig(3.c) [12,15].

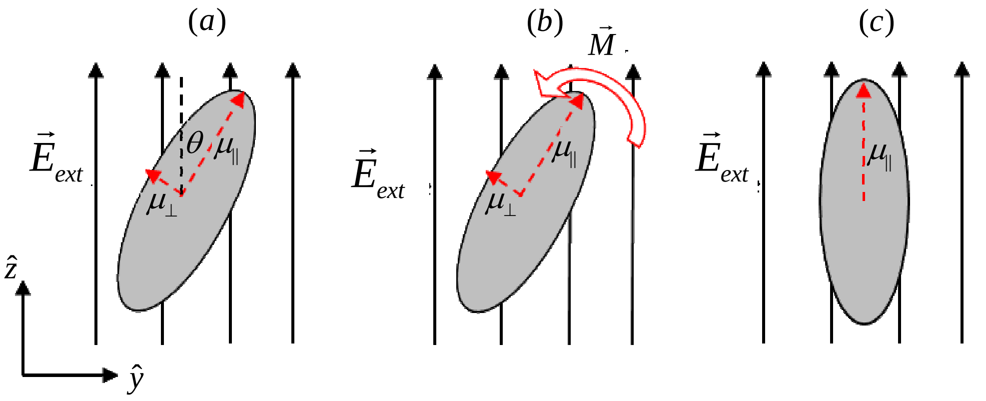

Fig 3. An illustration describing the alignment mechanism of the prolate spheroid, by a DC electric field: (a) The aligning field causes induced dipole moments $\mu_{\parallel},\mu_{\perp}$ in both spheroid major axes, parallel and normal respectively. (b) The induced dipole moments cause a rotating moment that acts on the spheroid. (c) The rotating moment align the spheroid parallel to the aligning field.

The result for the total rotating moment acting on a prolate spheroid is:

$$\begin{aligned}\vec{M} &= \vec{\mu}\times\vec{E} = \left(\alpha_{\parallel}\cdot E\cdot\sin\theta\right)\cdot\left(E\cdot\cos\theta\right)-\left(\alpha_{\perp}\cdot E\cdot\cos\theta\right)\cdot\left(E\cdot\sin\theta\right)\\ &=\left(\alpha_{\parallel}-\alpha_{\perp}\right)E^{2}\cdot\sin\theta\cdot\cos\theta\end{aligned} \tag{2.5}$$

The rotating moment is zero at two points: $\theta=0$ and $\theta=\pi/2$ but $\theta=\pi/2$ is an unstable point. Further on I will consider thermal fluctuations that enable me to ignore this point.

2.1.3 Hyperpolarizability

When a material has a NL susceptibility, an inclusion of that material under an electric field will response not only linearly (which is manifested by the polarizability) but also nonlinearly. The NL response in characterized by the hyperpolarizability. The two first orders of the hyperpolarizability β and γ evolve from the second and third order NL susceptibilities $\chi^{(2)}$ and $\chi^{(3)}$, respectively:

$$\vec{\mu}=\alpha\cdot\vec{E}_{ext}+\beta\cdot\vec{E}_{ext}^{2}+\gamma\cdot\vec{E}_{ext}^{3} \tag{2.6}$$

It is important to mention that $\chi^{(2)}$ can appear only in materials that lack a center of inversion (noncentrosymmetric lattice) [16]. I will ignore higher order nonlinearities in all further discussions. The NL process can excite a response from different field components, resulting in β and γ being third and forth rank tensors respectively, with a much more complicated presentation compared to the linear response, α. In section 6.1.2, I will discuss the tensorial behavior of the third order NL susceptibility.

Sihvola presents the solution for the hyperpolarizability of a sphere inclusion [7]. By expanding the polarization density in a power series of the internal field, and using a pertubative approach, he uses the linear internal field to describe the internal field in the power series. I will present only the result for the second order hyperpolarizability (third order nonlinearity). Using the same approach for an ellipsoid, by using the internal field in an ellipsoid instead of that of the sphere, the derivation is straightforward:

$$\gamma^{j}_{ellipsoid} = V\left(\frac{\varepsilon_h}{\varepsilon_h + L^j\left(\varepsilon_i - \varepsilon_h\right)}\right)^4 \varepsilon_0 \chi^{(3)} \tag{2.7}$$

Again the indices j represent the different direction regarding the ellipsoid major axes, ignoring the anisotropy properties of the susceptibility itself. In Appendix B, I present Sihvola's derivation for hyperpolarizabilities of a sphere and the generalization for the case of ellipsoids. I ignore any influence of the NL response of the inclusions on the rotating moment.

2.2 From single inclusion to a homogeneous mixture

My objective is to characterize a composite that has NRs dispersed in it. The main characterization I am interested in is the permittivity and third order NL susceptibility of the composite. In the linear regime of discussion, the basic model that deals with such a composite is the Maxwell-Garnett (MG) model [17]. The model analyzes a composite of spherical metal inclusions embedded in a dielectric material, when the inclusions are much smaller than the wavelength of the electric field that propagates through the composite (Fig. 4). Such a topology ensures that propagation along one wavelength encounters many inclusions, and the composite can be treated as a continuum [7]. I will address the details of the conditions for the MG model later on (section 3.1). Despite the fact that MG model and other models alike, deal with metal inclusions, the derivation for dielectric inclusions is the same [18].

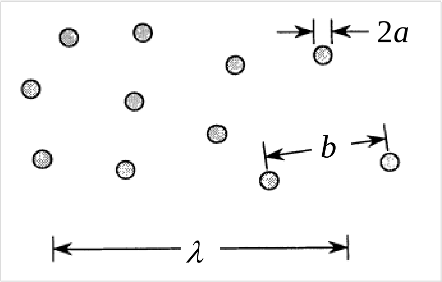

Fig. 4 – the composite topology in the MG model $a << b << \lambda$. Figure taken from [19].

2.2.1 Linear optical response

There are several methods presented by different authors for the derivation of the MG model (see for example [6,7,17,19]), all result with the same formula. In Appendix C, I present the derivation given by Sihvola, as an example. The result for the effective permittivity of such a composite is:

$$\varepsilon_{eff} = \varepsilon_h \frac{\varepsilon_i(1+2p) - 2\varepsilon_h(p-1)}{\varepsilon_h(2+p) + \varepsilon_i(1-p)} \tag{2.8}$$

where $\varepsilon_h, \varepsilon_i$ are again the host and inclusion permittivities respectively and p is the volume fraction of the inclusions from the whole composite. The validity limit of the MG model is up to $p = 20\%$ (see for example [6]).

There are several generalizations of the MG model, for cases of nonlinear (NL) inclusions and/or host and for the case of anisotropic inclusions. Gehr and Boyd published a review about the different models for the different cases [18]. For the case of ellipsoid inclusion, the depolarization factor is used, and the effective permittivity of the composite is [6,7]:

$$\varepsilon_{eff}^{j} = \varepsilon_h + p \cdot \varepsilon_h \frac{\varepsilon_i - \varepsilon_h}{\varepsilon_h + L^j (1-p)(\varepsilon_i - \varepsilon_h)} \tag{2.9}$$

In order to understand the influence of the different parameter inside Eq. (2.9), I present them graphically in Fig. 5, for the LA direction. For each case, I examine the result changing one parameter, when holding the three others constant (ε_i, L^j, p). The constant values are: $\varepsilon_i = 6.2$, $L^{\parallel} = 0.25$, $p = 0.1$. The value of the host permittivity was set on $\varepsilon_h = 2.19$ for all three graphs.

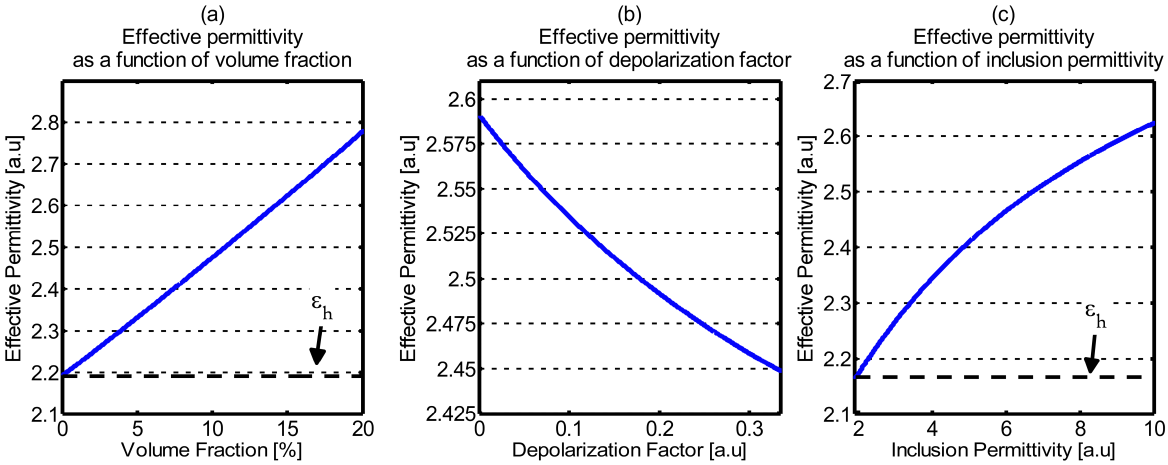

(a) Effective permittivity as a function of volume fraction

(b) Effective permittivity as a function of depolarization factor

(c) Effective permittivity as a function of inclusion permittivity

Fig 5. Influences of the different parameters on the effective permittivity of the composite: (a) Volume fraction, from 0 to 20% - the MG model limit. (b) Depolarization factor of the LA, from 0 to 1/3. (c) Inclusions permittivity, from ε_h to 10.

As expected, more NRs in the composite, meaning larger volume fraction, will influence the composite to have a permittivity which approaches to that of the NRs themselves (Fig. 5.a). Regarding the depolarization factor, the smaller the LA depolarization factor is (i.e large axes AR), the larger will be the effective permittivity (Fig. 5.b). We can see from here that for shapes like a needle, the permittivity will be larger, in contrast to sphere-like inclusions that have smaller effective permittivity. The permittivity of the inclusions increases the effective permittivity (Fig. 5.c).

2.2.2 Non-linear optical response

As mentioned, Gehr and Boyd published a summary for different models dealing with composites' macroscopic characteristics, both linear and NL [18]. Later on Sihvola presented a model for NL sphere inclusions [7] and Lamarre *et al.* presented a model for NL ellipsoid, for both small and large volume fraction (up to the MG model limit) [6]. The models of Sihvola and Lamarre *et al.* converge in the case of small volume fraction with sphere inclusions. In Appendix D, I present the different approaches for the derivation and the basic assumptions in each one. I will use the method presented by Sihvola, for derivation of the effective third order NL susceptibility for composites with ellipsoid inclusions. I chose to use this derivation, which will be convenient for partially aligned nanorods composite latter on. The third order NL susceptibility for small volume fraction composite with ellipsoids is:

$$\chi_{eff}^{(3),j} = p\left(\frac{\varepsilon_h}{\varepsilon_h + L^j\left(\varepsilon_i - \varepsilon_h\right)}\right)^4 \chi_i^{(3)} \tag{2.10}$$

where $\chi_i^{(3)}$ is the third order NL susceptibility of the ellipsoids and again, the index $j = x, y, z$ denotes the different major axes of the ellipsoid. Two important things to notice: (a) The whole expression can be written as $\chi_{eff}^{(3),j} = n \cdot \gamma^j / \varepsilon_0$ where n is the number density of the ellipsoid inclusions in the composite, which satisfies $n \cdot V = p$ and γ^j is the second order hyperpolarizability presented in Eq. (2.7). (b) In the macroscopic equations, Eqs. (2.8)- (2.10), the volume of the single NR is of no consequence; rather the important parameter is the volume fraction, p.

The dependencies of the effective third order NL susceptibility of the composite for the LA direction are presented in Fig. 6. The results are for the effective third order NL susceptibility, normalized by that of the inclusions, for simplicity. The constant values are same as in Fig. 5.

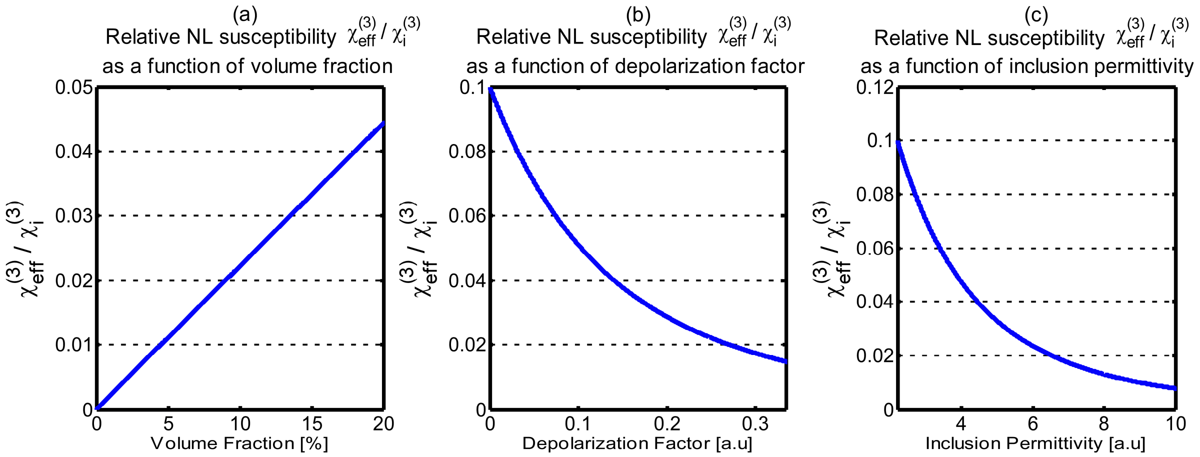

Fig 6. Influences of the different parameters on the effective third order NL susceptibility of the composite normalized by that of the inclusions: (a) Volume fraction, from 0 to 20% - the MG model limit. (b) Depolarization factor of the LA, from 0 to 1/3. (c) Inclusions permittivity, from ε_h to 10.

The first two dependencies on volume fraction and on the depolarization factor, Fig. 6.a and 6.b, are similar to the dependencies in the effective permittivity (Fig. 5.a and 5.b). For the volume fraction it is a perfect linear dependency (Fig. 6.a), as can be seen from Eq. (2.10), for the reason that only the inclusions contribute to $\chi_{eff}^{(3)}$. For the depolarization factor, once again, the smaller the depolarization factor is the larger will be the effective susceptibility (Fig. 6.b). However, the dependency on the inclusion permittivity is opposite to that of the effective permittivity (Fig. 6.c).

3. Research framework and methodology

3.1 Basic assumptions

3.1.1 Electrodynamics and the quasi-static approximation

As explained in section 2.2.1, the basic assumption of all models based on the MG model is small size inclusions relative to the wavelength of the electric field in question. Sipe and Boyd set a limit on the wavelength requirement, being much bigger than the distance between particles that is much bigger than the particles size (see Fig. 4 from [19]). Sihvola used the "quasi-static approximation" for the homogenization in the MG model, which means that the internal field inside the inclusions is uniform [7]. As a "rule of thumb" he sets the limit $\lambda/2\pi > a$, where a is the typical size of the inclusions. Both limitations express the idea that the electric field varies much slower (spatially) than the permittivity differences inside the medium it propagates in, hence the medium can be treated as continuum, i.e homogenization of the mixture. The ultimate goal of this work, is an optical WG that operates in the telecommunication C-band, and I will use $\lambda = 1550nm$ as the wavelength for my computations. I will use the wavelength in the host material ($n_h = 1.479$, ignoring the composite effective values) – $\lambda/n = 1050nm$. The limit set by Sipe and Boyd is very restrictive and can be referred to as $a < 10.5nm$, where a can be treated as the length of the NRs. Using Sihvola's limit, the length requirements of the NRs is relaxed and should be smaller than $\sim 160nm$. I will adopt the limit introduced by Sihvola, which allows me to avoid the quantum confinement region, as will be explained in section 3.1.3 ahead.

3.1.2 Optical interactions

In the interaction of the optical field or photons with the NPs, for the linear regime of discussion, I ignore direct transitions (i.e absorption). This is justified for some semiconductors, depending on their bandgap, if it is higher than the energy of a photon in the wavelength of $\lambda = 1550nm$ (see Fig. 8 ahead, circles for bulk material bandgap).

In the NL regime, I am interested in effects evolving from the Kerr-type nonlinearity, such as self phase modulation and self focusing. A competing process to those processes is two-photon-absorption (TPA), which can be a strong effect for relatively low band gap material (e.g Silicon for wavelength of $\lambda = 1550nm$ [20,21]). In order to decrease the influence of

TPA, the NR material should be with bandgap that exceeds the energy of two photons, but does not go far above it, otherwise the Kerr-type nonlinearity effects start to decrease as well (see e.g Fig. 7 from [16] and Ref. [20] for silicon).

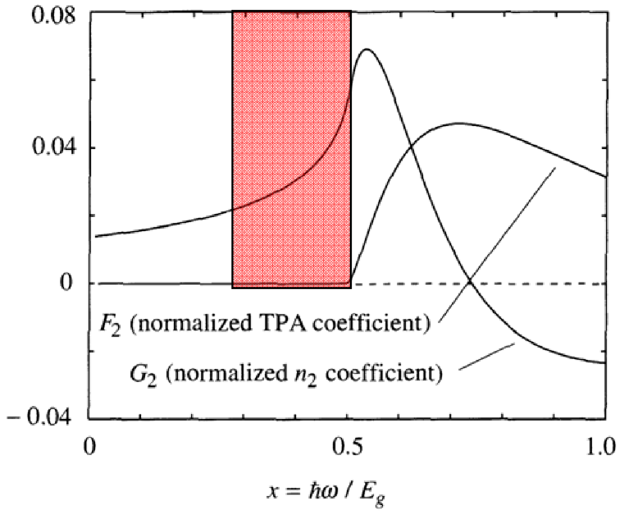

Fig 7. The influence of the bandgap on the efficiencies of TPA and Kerr-type nonlinearities (expressed by the intensity dependent refractive index n_2). For a bandgap approaching twice the photon energy (x=0.5) the TPA approaches zero and n_2 becomes maximum. For larger bandgaps (x<0.5) the TPA is zero, but n_2 starts to decrease as well. Image taken from [16]. I added a shaded region (red) indicating the recommended operating regime for my purposes.

3.1.3 Quantum confinement

All of the works mentioned in the theoretical background, did not refer to quantum confinement effects that appear in NPs. The expression for the band gap for NPs is based on the bulk material band gap with supplements that evolves from the quantum confinement, which raises the band gap. The lower size limit of NPs, where quantum confinement effects start to be significant, is usually referred to as the Bohr radius of the bulk exciton $a_{exciton}$ [22]. If the NP has at least one dimension which is smaller than the Bohr radius of the bulk exciton, it cannot be treated as a classical particle anymore. Following all the authors mentioned before (see e.g [19] explicitly), I ignore all such effects in this work and use the bulk values for the material properties. In order to do so, I should consider only NRs with $SA > 2 \cdot a_{exciton}$, where $a_{exciton}$ is given by [23]:

$$a_{exciton} = a_0 \frac{m_e \varepsilon_r}{\mu^*} \tag{3.1}$$

where $a_0 = 0.053nm$ is the Bohr radius (derived for hydrogen), m_e is the rest mass of the electron, ε_r is the permittivity of the bulk material which is taken as the low frequency value and $\mu^* = m_e^* m_h^* / \left(m_e^* + m_h^* \right)$ is the reduced mass of the electron and hole effective masses in the bulk material.

Using values for CdSe, as an example: $\varepsilon_r = 10.2$, $m_e^* = 0.13 \cdot m_e$, $m_h^* = 0.45 \cdot m_e$, where the effective mass of the electron and hole were taken from [27]and [28], respectively. The result is $a_{CdSe} = 5.7nm$. Meaning NRs with minimum radius of $6nm$ or minimum width of $12nm$ are required.

3.2 Simulations method

Beside the theoretical derivations in this work, I performed simulations and numerical calculations. The simulations were executed for electrostatic analysis of single inclusions (e.g calculations of internal field, polarization density etc.) and for characterizing optical WGs in the linear regime (e.g optical field distribution in the WG core and clad). All these simulations were performed by finite element analysis (FEA) with COMSOL Multiphysics software.

3.3 Nanorods material selection

All of the analysis and results presented so far were for CdSe NRs. One of the reasons I chose to use the CdSe, is the extensive research done on CdSe NRs, including direct measurements of the permanent electrical dipole moment in them, as will be explained in section 4.2. As mentioned (section 3.1.2), a major requirement from the NRs materials relates to its band gap. In order to avoid TPA and enhance Kerr-type nonlinearities, the energy band gap of the NL material needs to be slightly above the resonance of the two photons energy. In Fig. 8, taken from [24], the bandgap energies of several semiconductor NPs are presented, including bulk value and the affect of quantum confinement. The level of

1.55µm photon energy is also presented and I added a line (blue solid line), representing the two photons energy for 1.55µm photon wavelength.

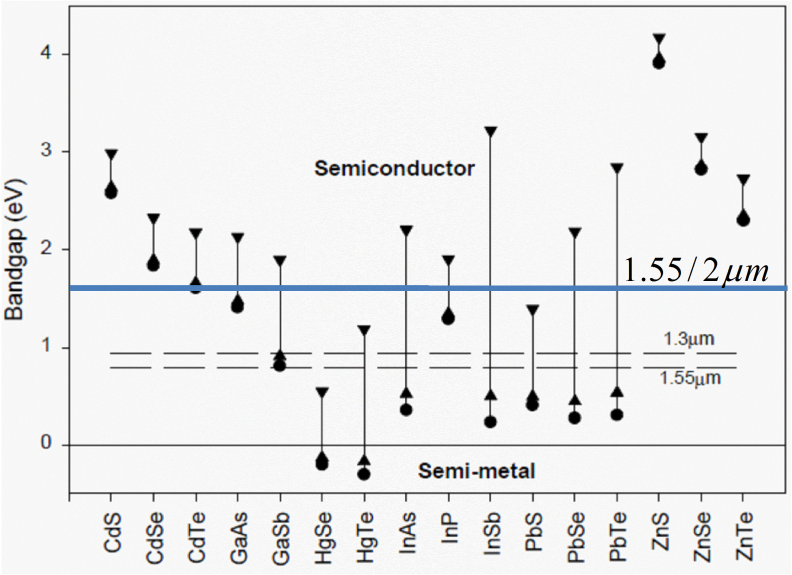

Fig 8. Dependence of bandgap energies (calculated) to particle size for a range of semiconductors. Bandgap are shown for the bulk forms (circles) and at a dot radii of 10 nm (up triangles) and 3 nm (down triangles). The energy levels for 1.55 and 1.3µm photons are also presented (dashed lines). Image source [24], I added the energy levels for two 1.55µm photons (blue line)

In addition to bandgap consideration, semiconductors with wurtzite lattice structure, which posses a permanent dipole moment (PDM) that can assist the alignment mechanism, are preferred as will be explained in section 5.2. Combining these two demands, for the bandgap and lattice structure, the choice with CdSe is justified:

CdSe NRs can be grown in wurtzite lattice structure, and their PDM was investigated thoroughly [25,26]. The band gap of CdSe is 1.73 eV, which is above and close to the TPA energy limit (1.6 eV). For comparison, CdS and ZnO, that also posses PDM, have bandgap energies of 2.42 and 3.37eV, respectively, which is much higher, hence the Kerr-type nonlinearities will start to decrease.

It is important to note that the wurtzite lattice structure is noncentrosymmetric, meaning it can present second order nonlinearities. I will ignore such nonlinearities in this work.

4. Prolate spheroid versus capsule shape description

4.1 Geometrical description

Most authors dealing with NR analytical calculations treat them as prolate spheroid (see illustration in Fig. 10.a). Prolate spheroids have a closed form for their depolarization factor and analytical solution can be found both for the polarizability and the generalized MG model. However, most TEM images published, for colloidal NRs, show a different shape (see for example Fig. 10.b from [29] and Ref [30]). The shape is more like a cylinder with round capping. I wish to propose a "capsule shape" description for the single NR, meaning a cylinder with hemisphere capping, as illusrated in Fig. 10.c.

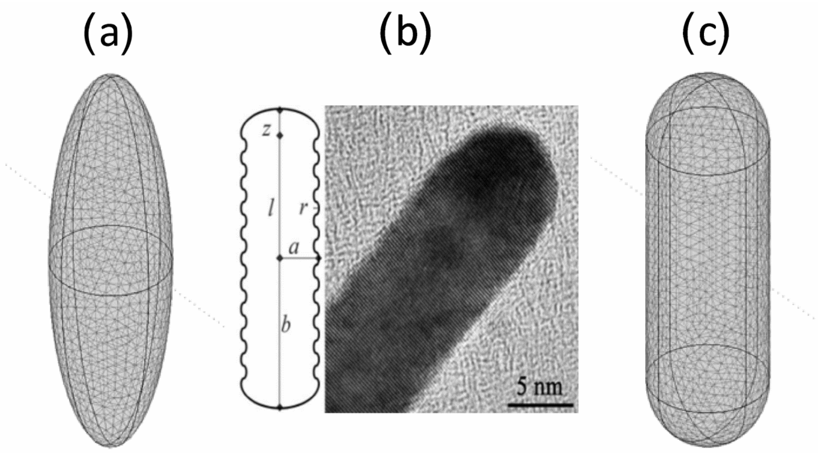

Fig 10. NR geometry: (a) A prolate spheroid. (b) Outline showing the geometry of the cylinder and the capping geometry and high-resolution electron micrograph of a single gold rod (taken from [29]). (c) A capsule shape – a cylinder with hemisphere capping. Length and width of the capsule are equal to that of the spheroid in (a).

Pecharromán *et al*. analyzed the geometry of different shapes, mainly cylinder and capped cylinders, in order to calculate the extinction spectra of small metal particles of different shapes [29]. They showed geometrical structure of different NRs with different capping. They also refer to the roughness of the surface of the NRs and claimed that both the exact capping geometry and the roughness can affect the surface plasmon peak energy. In order to avoid further complication and enable a model that combines numerical and analytical calculation, I will ignore the roughness and different capping geometry in my work. I will refer to all NRs as cylinder with perfect hemisphere capping, with a radius equal to that of the cylinder. In Fig. 11, I present an illustration that demonstrates the dimensions of the prolate spheroid compared to that of the capsule shape.

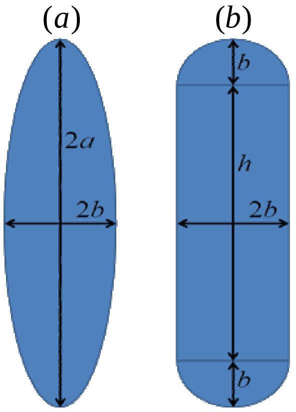

Fig 11. Prolate spheroid and capsule shape geometry: (a) A prolate spheroid with semi-axes of a and b. (b) A capsule shape composed of: (1) a cylinder with height $h = 2(a - b)$ and radius $r = b$ (2) two hemisphere capping with a radius of $r = b$. The total length and width of both shapes are the same: $L = 2a$, $W = 2b$.

In the next sub-sections I will analyze the electrostatic characteristics of the capsule shape and compare them to that of a prolate spheroid with the same length and width.

4.2 Polarizability

I first wish to analyze the polarizability of the proposed capsule shape geometry. I simulate different sizes of capsule shapes, both with varying ARs and varying volumes. From the simulations, I extract the polarization density, and integrate over the volume (see Eq. (2.1)) to find the induced dipole moment in the capsule shape inclusion. Then by using the definition of the polarizability $\vec{\mu} = \vec{\alpha} \cdot \vec{E}_{ext}$, I can calculate the polarizability. As explained, the anisotropy of the polarizability is due to the geometry of the inclusion alone. Most authors that dealt theoretically with prolate spheroids, presented the polarizability as a diagonal [3×3] matrix, with two equal elemnts (for the two equal SAs). My simulations,for the prolate spheroids, resulted also with off-diagonal elemnts, but they were six orders of magnitude smaller. The off-diagonal elemnt might be real or an artifact of the FEA simulation and I will ignore them. For simplicity of the comparison, I present the results for an electric field linearly polarized along the inclusion LA, hence only one component of the polarizability tensor is presented. The results for polarization along the SA are not presented, in order to stay concise. I compared the results of simulation of prolate spheroid and of the capsule shape with the same length and width. Table 1 presents examples of the simulation results, with the results of the polarizability of the prolate spheroids according to Eq. (2.2), in order to evaluate the simulation results. I added also the results of the polarizability normalized by the volume, which can be treated as a measurement for the polarization density in the inclusions.

Table 1. Polarizability of capsule shape. A comparison between the analytical and simulation results of the polarizability of different axes length prolate spheroids and the simulation results of equal axes length capsule shapes. Results for the polarizability normalized by the inclusion volume are also presented, for the simulation results only. The permittivity of the host and inclusions were set on $\varepsilon_h = 2.4$, $\varepsilon_i = 10.2$ respectively. Polarizability calculated along the inclusion LA.

No	l $[nm]$	d $[nm]$	Aspect Ratio	$\alpha/(4\pi\varepsilon_0)$ $\left[nm^3\right]$			$\left[\alpha/(4\pi\varepsilon_0)\right]/V$	
				Spheroid (analytical)	Spheroid (Simulation)	Capsule (Simulation)	Spheroid (Simulation)	Capsule (Simulation)
1	8	2	4	8	8	11	0.499	0.487
2	40	10	4	1,044	1,044	1,402	0.499	0.487
3	40	8	5	704	704	958	0.525	0.511
4	40	4	10	195	195	274	0.582	0.564
5	60	6	10	659	659	924	0.582	0.564

The average error of the simulations for the polarizability of the spheroids regarding to the analytical formula (Eq. (2.2)) is 0.02%, which is very good result. The results for the polarizability of the capsule shapes are substantially larger than those for the prolate spheroid shapes. The average deviation is 37% in favor to the capsule shape. However the results for the normalized polarizability of the capsule shapes are slightly smaller than those of the prolate spheroid shapes, with an average deviation of 2.8%. The larger polarizability of the capsule shape is due to the its larger volume. The volume of the capsule shapes are 35-50% larger than those of the prolate spheroid shapes, with the same length and width (AR dependent). As a result of the large volume the polarizability is larger despite the slightly smaller polarization density.

In addition, it can be seen that equal axes AR shapes have the same normalized polarizability, both for the prolate ellipsoids and for the capsule shapes. I highlighted rows with equal AR – rows 1 with 2 (blue) and 4 with 6 (red). The reason is that the polarizability depends linearly on the volume, dependency that is reduced in the normalized polarizability. The normalized polarizability dependency on the geometry, for the same general shape, is due to the AR alone.

In order to better understand the behavior of the polarizability of the capsule shapes, I will assume a similar behavior as in the case of the prolate spheroids – a dependency in the different permittivities (which are constants) and the AR, multiplied by the volume. Again this is consistent with the equal values of polarizability normalized by the volume, for the same AR, as explained. Since I defined the AR as LA/SA, while Eq. (2.3) uses the reciprocal term SA/LA, I present the normalized polarizability versus AR^{-1}. The results for the capsule shapes and the prolate spheroid shapes are plotted in Fig 12 with the analytical curve for the prolate spheroids and a quadratic fit curve for the capsule shapes.

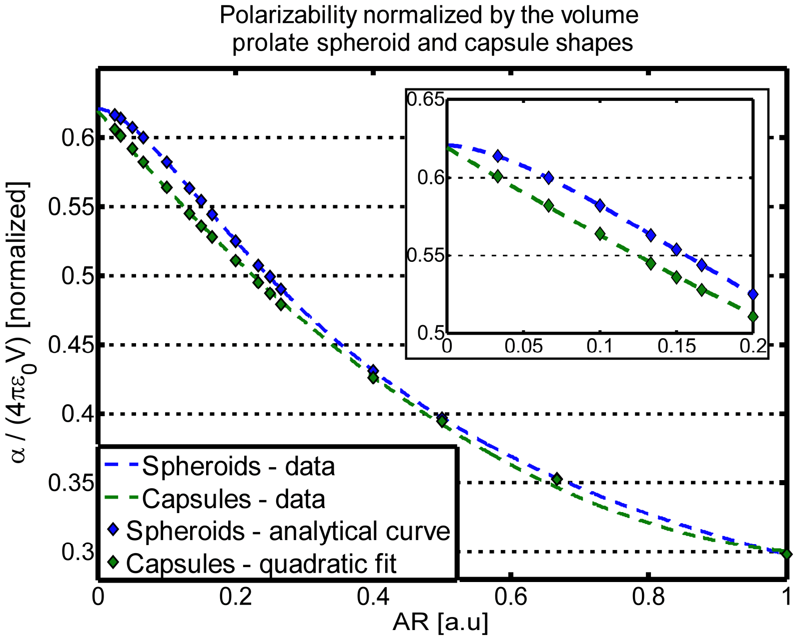

Fig. 12: The polarizability normalized by the volume as a function of AR^{-1} for prolate spheroid, with the analytical curve, and for capsule shapes, with a quadratic fit curves. Inset: zoom in on high AR values.

The values of the normalized polarizability of the capsule shapes are smaller in compare to those of the prolate spheroid shapes, as can be seen in Table 1. The two curves converge, both for the value of AR=1, meaning a sphere, and for very high AR values ($AR^{-1} \rightarrow 0$, see inset), which is the value for a needle shape (LA depolarization factor – zero). The R-square of the quadratic fit for the capsule is 0.9995, which is an excellent match, meaning for a given host and NRs permittivities, I can calculate the NRs normalized polarizability by extrapolating or interpolating the quadratic curve for the capsule shape.

After calculating the normalized polarizability it can be multiply by the volume, to achieve the polarizability itself.

4.3 Depolarization factor

In order to use the results of the capsule shapes polarizability in the equations for the macroscopic characteristics of a composite (the effective permittivity and third order NL susceptibility – Eqs. (2.9) and (2.10)), I need to calculate the depolarization factor of the capsule shape inclusions. Since there is no analytical formula for that, I will find an equivalent prolate spheroid for each capsule shape, regarding its polarization density or normalized polarizability. I use the results for the normalized polarizability, presented in Table 1, inside Eq. (2.2) in the form:

$$\frac{\alpha}{V} = \varepsilon_0 \frac{\left(\varepsilon_i - \varepsilon_h\right)}{\varepsilon_h + L^j\left(\varepsilon_i - \varepsilon_h\right)} \varepsilon_h \qquad 4.1$$

Using the values for the permittivities and the results from the simulation for α/V, I can extract the depolarization factor L^j .This is not a real analytical value for the depolarization factor, rather an effective value. In table 2, I present the results for the effective value of the depolarization factors of the capsule shapes presented in table 1.

Table 2. Effective value for capsule shapes depolarization factor. The values of the AR and depolarization factor for different axes prolate spheroid and the effective depolarization factor values for the equal axes capsule shape are presented. Results for the same conditions as in Table 1.

No	l $[nm]$	d $[nm]$	Prolate Spheroid Aspect Ratio	Depolarization Factor	
				Prolate Spheroid – analytic	Capsule Shape – effective value
1	8	2	4	0.0754	0.0838
2	40	10	4	0.0754	0.0844
3	40	8	5	0.0558	0.0648
4	40	4	10	0.0203	0.0307
5	60	6	10	0.0203	0.0305

First we can see from Table 2 that the capsule shape depolarization factor cannot be determined solely by the AR. Different volume (axes length) capsule shape, with same AR do not have exactly the same effective depolarization factor, in contrast to prolate spheroids. The reason for that is unknown; however the deviation between the values of the depolarization factor (for same AR capsule shape) is small (less than 1%). This means that by approximation I can determine the effective depolarization factor of the capsule shape by the AR, as presented by Table 2. In addition, the values of the depolarization factor of the capsule shapes are larger than those of the prolate spheroids (again for same AR capsule shape).

After calculating the capsule shape depolarization factor, the macroscopic characteristics of a composite can be calculated as well, using Eqs. (2.9) and (2.10). As explained regarding Fig. 5 and 6, bigger depolarization factor means smaller effective permittivity and effective third order NL susceptibility for composites. This means that the values for ε_{eff} and $\chi_{eff}^{(3)}$ calculated using the model of capsule shapes will be lower, comper to those calculate using the model of prolate spheroids, given a certain volume fraction. In addition, since the volume of a prolate spheroid is smaller than that of a capsule shape (with the same AR), a given volume fraction means the number of spheroids will be bigger than the number of capsule shapes. Once again it is important to remember that the volume of the single inclusion and the number of inclusions are irrelevant for the effective macroscopic characteristics, rather the volume fraction and single inclusion depolarization factor. As long as I maintain the depolarization factor (determined by the AR), large number of small inclusions or small number of large inclusions will result with the same outcome.

5. Alignment and statistical behavior of NRs

5.1 Rotating moment on capsule shape NRs

The rotating moment on a prolate spheroid was presented analytically in section 2.1.2. In order to calculate the rotating moment on a capsule shaped particle, the only modification needed, is to use the capsule shape polarizability, as presented in section 3.2.2, within Eq. (2.8) for the rotating moment: $\vec{M} = \vec{\mu} \times \vec{E}_{ext}$. I will use the notation $\alpha_{\|}$ and $\alpha_{\perp}$ for the polarizability in the parallel (LA) and normal (SA) directions respectively. As shown in Fig. 3, the external electric field is oriented in the $\hat{z}$ axis hence the capsule shape dipole moment will be in the $\hat{y}-\hat{z}$ plane when the LA is with an angle θ regarding the $\hat{z}$ axis. The rotating moment will be:

$$\begin{aligned} \vec{M} &= \vec{\mu} \times \vec{E} = \left(\alpha_{\|} \cdot E \cdot \sin\theta\right) \cdot \left(E \cdot \cos\theta\right) - \left(\alpha_{\perp} \cdot E \cdot \cos\theta\right) \cdot \left(E \cdot \sin\theta\right) \\ &= \left(\alpha_{\|} - \alpha_{\perp}\right) E^2 \cdot \sin\theta \cdot \cos\theta \end{aligned} \tag{5.1}$$

5.2 Permanent dipole moment

Our intention is to insert NRs into a PFCB polymer in liquid form and align the NRs along a preferred direction. The alignment mechanism is an applied DC electric field that will align the NRs parallel to its direction, as explained at section 2.1.2. After doing so, the PFCB will be thermally polymerized in order to achieve a solid form of the composite, locking the NRs in place. The problem with such a process is that the polymerization is made at thermally elevated temperatures of 120-350°C [31], which increases the thermal fluctuations in the NRs direction [12]. I will refer to the temperature limit under which nanocrystals are stable, later on (section 6.2.3); for now, I will assume a temperature of 150°C, applicable for PFCB. The alignment process can be significantly enhanced (thus better coping with thermal fluctuations) by doping with NRs possessing a permanent dipole moment (PDM). Large PDMs were found mainly in wurtzite lattice structure NRs [25,26]. Nann and Schneider presented a model which explains the PDM by small deviations of the crystallographic structure from the ideal wurtzite lattice structure [26]. Li and Alivisatos investigates CdSe NRs with wurtzite lattice structure and measured a large PDM in them – around 100-200 Debye [25]. The PDM is directed along the c-axis in the hexagonal lattice, which is also the long axis of the NR itself. The presence of such a PDM can help the alignment mechanism, since the rotating moment depends linearly on the dipole moment in the NR.

Li and Alivisatos, estimated the PDM by transient electric birefringence (TEB) experiments. TEB experiment examines the rising and falling of the birefringence upon application and removal of an external electric field, respectively. The TEB curves rising and falling is fitted to the theoretical formula and from the fitting, the polarizability anisotropy is extracted. The polarizability anisotropy is defined as:

$$\Gamma = \frac{\mu_z^{'2}}{K_B T\left(\alpha_{\parallel} - \alpha_{\perp}\right)} \tag{5.2}$$

where $\mu_z^{'2}$ is the value of the permanent electric dipole moment (screened by surface effects) along the long axis of the rods, $\alpha_{\parallel}, \alpha_{\perp}$ are the polarizability parallel and normal to the LA, respectively.[1] By computing Γ from the TEB curves and calculating the polarizability in the different directions, the PDM $\mu_z^{'2}$ can be calculated. Li and Alivisatos calculated the PDM using the analytic polarizability of a prolate spheroid presented by Landau & Lifshitz (see section 2.1 and Appendix A) [25]. According to my analysis of NRs geometry as capsule shapes, I found that the polarizability is larger. I used the data presented by Li and Alivisatos with my analysis for capsule shape polarizability. The permittivity of the surrounding and CdSe NRs in both directions are: $\varepsilon_h = 2.02$, $\varepsilon_{\parallel} = 10.2$, $\varepsilon_{\perp} = 9.33$ and the dimensions of the NRs are presented in Table 3. I simulated capsule shaped NRs under those condition, calculated the polarizability in both direction and from the polarizability anisotropy calculated the PDM of the NRs. In Table 3 I present the results for the PDM; the results presented in Li and Alivisatos work, results calculated from the polarizability formula given by Sihvola and my calculations according to the capsule shape analysis.

---

[1] In the article, the polarizability anisotropy is marked as γ . I changed it to Γ to avoid confusion with the second order hyperpolarizability.

Table 3. PDM values for different dimensions CdSe NRs. A comparison between the values calculated according to the polarizability formula given by Landau and Lifshitz (denoted L&L and presented by Li and Alivisatos), those calculated according to the polarizability formula given by Sihvola and those calculated for capsule shapes. The induced dipole moment, for an external field of $E = 10^7\,V/m$ is also presented. Values for the permittivities: $\varepsilon_h = 2.02$, $\varepsilon_{\|} = 10.2$, $\varepsilon_{\perp} = 9.33$

L [nm]	W [nm]	PDM – μ [Debye]			$\mu_{\|}^{induced}$ $[Debye]$ $\left(E = 10^7\,V/m\right)$
		Spheroid L&L formula	Spheroid Sihvola formula	Capsule Calculated	
60	3.1	153.4	218.0	249.9	101.6
30	4.8	209.9	298.3	329.8	104.0
23	3.8	126.4	179.6	198.3	49.6
54	3	126.3	179.5	205.4	85.0
35	3	95.7	136.0	153.7	52.8

Using the polarizability formula given by Sihvola, increases the PDM results in a factor of $\sqrt{\varepsilon_h}$ (increase by 42% in the table). Using the capsule shape analysis, increase the original result by average of 60%. From a linear curve of the resulted PDM versus the NRs volume, the permanent polarization density can be calculated. The results presented by Li and Alivisatos shows a permanent polarization density of 0.19µC/cm^2. Calculating by the formula given by Sihvola results with permanent polarization density of 0.26µC/cm^2, while from the capsule shape analysis the value is 0.205 µC/cm^2.[2] The predicted value by Schmidt *et al.* is 0.6 µC/cm^2 (phenomenological rule, proven experimentally for ferroelectric materials [32]) and by Nann and Schneider is 0.42 µC/cm^2 [26].

For the same NRs dimensions, the results for the induced dipole moment are much smaller. Looking at the results for the induced dipole moment in the parallel direction, under a DC field of 10^{7}V/m, the results are 2.5-4 times smaller, as can be seen in the last column of Table 3. These high values of PDM will enhance the alignment of the NRs.

---

[2] The larger value for the analysis by the formula given by Sihvola evolves from the smaller volume of the prolate spheroids.

5.3 Angular distribution function

To find the statistical distribution of the alignment of the NRs, I will use the method presented by Ruda and Shik [12]. They calculated the angular distribution function (ADF) of NRs under different kinds of electric fields: DC, AC and DC+AC, where the field is uniform over the whole composite. I will use the DC electric field alignment model, which is the strongest. They used the rotating moment $\vec{M}$ acting on a NR with an angle θ to the aligning electric field, calculated in section 2.1.2, which is a function of the angle θ. They calculated the potential energy of the single NR, which equals the work done to bring the NR to this angle from the minimum energy position $\theta = 0$:

$$U_{NR}\left(\theta\right) = W_{0\to\theta} = \int_0^{\theta} M\left(\hat{\theta}\right)\cdot d\hat{\theta} \tag{5.3}$$

After calculating the single NR potential energy for an arbitrary angle, the ADF can be derived by:

$$ADF\left(\theta\right) = \frac{\exp\left(-\frac{U_{NR}\left(\theta\right)}{K_B T}\right)}{\int_0^{\pi} \exp\left(-\frac{U_{NR}\left(\hat{\theta}\right)}{K_B T}\right)\sin\hat{\theta}\cdot d\hat{\theta}} \tag{5.4}$$

The integration boundaries in the denominator need careful treatment. As explained (section 2.1.2), the angle θ is a tilt angle, between the applied electric field and the direction of the NR LA (see Fig. 3.a). This angle is normally defined over the interval $\theta = \left[0,\pi\right]$. However for the case of a shape that its geometry has symmetry to rotation by π (like spheroids and capsule shapes) the integration boundaries is usually set on $\theta = \left[0,\pi/2\right]$ as done by Ruda and Shik [12]. The is that the energy is degenerated for the states of a tilt in θ and a tilt in $\theta+\pi/2$. However, when considering the case of the presence of PDM in the NRs, the two ending of the LA of the NR are distinguishable, hence the symmetry reduces. The energy degeneration is removed and the integration boundaries are set on $\theta = \left[0,\pi\right]$. As explained in section 2.1.2, the entire analysis can be done in the plane defined by the electric field and the NR LA as shown in Fig. 2.b. The azimuthal angle φ in the $\hat{x}-\hat{y}$ plane (see Fig. 2.a) can be ignored for now, due to the degeneracy of the NRs geometry, which has 2 equal SAs. I will refer to it later on (see section 6.1.1).

Ruda and Shik used the analytical result for the rotation moment on a prolate spheroid (Eq. (2.5)) using the Landau & Lifshitz formula for the polarizability (see again section 2.1.1 and Appendix A). I will use the results for the polarizability of the capsule shapes, as explains in section 4.2. In addition to using the capsule shape result, I will add the influence of the PDM on the rotating moment and potential energy. Given that the different induced dipole moments are $\mu_{\parallel} = \alpha_{\parallel} E \cdot \cos\theta$, $\mu_{\perp} = \alpha_{\perp} E \cdot \sin\theta$ and the PDM is μ_{PDM} which is also assumed in the parallel ($\hat{z}$) direction, Eq. (5.1) becomes:

$$\vec{M} = \vec{\mu}_{total} \times \vec{E} = \left(\alpha_{\parallel} - \alpha_{\perp}\right) E^2 \cdot \sin\theta \cdot \cos\theta + \mu_{PDM} E \cdot \sin\theta \tag{5.5}$$

The potential energy of the single NR will be computed according to Eq. (5.3) :

$$U_{NR}\left(\theta\right) = \left(\alpha_{\parallel} - \alpha_{\perp}\right) E^2 \cdot \sin^2\theta - \mu_{PDM} E \cdot \cos\theta \tag{5.6}$$

Since the expression $\left(\alpha_{\parallel} - \alpha_{\perp}\right)$ is always positive (semiconductor with elongated shapes) the minimum of the energy will be at $\theta = 0$. After calculating the single NR potential energy, I calculate the ADF. Fig. 13 shows the ADF of NRs with the dimensions shown at Table 3, under different conditions. First, the influence of the aligning electric field strength for NRs with just induced dipole moment (Fig. 13.a) and for NRs with both induced and permanent dipole moment (Fig. 13.b) is shown. In both of them I compare the results for prolate spheroid and for capsule shapes, for different aligning field strengths. Fig. 13.c presents the dependency in the temperature again for different aligning electric field strengths. All three images (Fig 13.a-c) are for temperature of 150^{o}C and for the largest NR in Table 3 $\left(L = 30nm\ , W = 4.8nm\right)$, which has the largest value of PDM. In Fig 13.d I present the influence of the volume of the NRs on the ADF.

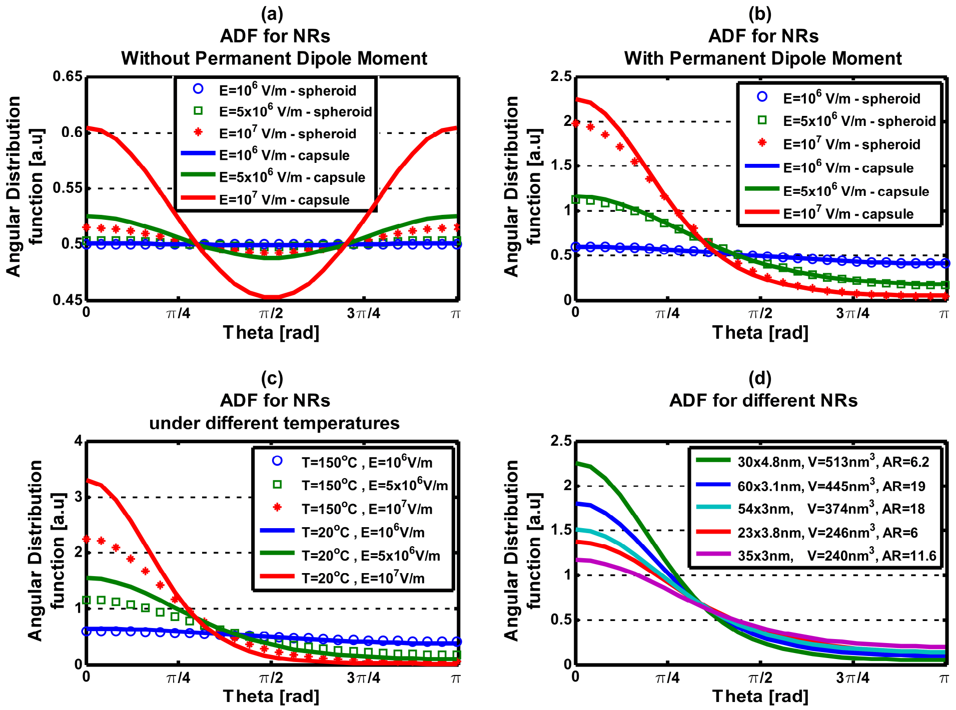

Fig. 13: (a) ADF of CdSe NRs without PDM inside PFCB, capsule shape versus prolate spheroid for different aligning electric field strength under temperature of 150°C, $l = 30nm$, $d = 4.8nm$ (b) The same for NRs with PDM. (c) Temperature dependency for different aligning field strengths (with PDM). (d) Different NRs with different volume (for the NRs presented in Table 3, with PDM).

As explained, with the presence of the PDM the ADF symmetry breaks and there is no longer symmetric for rotation in π, as can be seen at Fig. 13.b compared to Fig 13.a. In both figures, the capsule shapes have larger induced dipole moment (solid line), compared to the prolate spheroids (discrete markers), hence the alignment is stronger. Lower temperature (Fig. 13.c) results in stronger alignment, due to lower thermal fluctuations, and larger NR volume (Fig. 13.d) make the alignment stronger as well. The rotating moment aligning the NRs depends on their polarizability and PDM, which depend linearly on their volume. Hence, for the alignment mechanism the single NR is a major parameter that influences the results, in contrast to the composite characteristics which depend on the inclusions fractional volume. The composite characteristics will be controlled by the alignment degree, together with the AR influence, which will be investigated in section 6.2.2.

6. Partially aligned composite characteristics

In this section I present the core of my work. In the former sections, I explained the model for nematic array of prolate spheroid. Afterwards I explained the method of using the capsule shape model – both for the polarizability and for extracting an effective value for the capsule shape depolarization factor. Lastly, I introduced the alignment mechanism and the modifications for using it with capsule shapes and the presence of a PDM. The goal of this section is to combine the understanding of the statistical behavior of the directionality of the NRs, into the model for the nematic array. I will examine the permittivity and third order NL susceptibility of a composite, in which the NRs has a certain alignment distribution, with a preferred direction.

6.1 Permittivity and NL susceptibility for partially aligned composite

6.1.1 The linear response – permittivity

Sihvola presented an integral form of the average polarization density in such a composite, without explicit derivation of the effective permittivity [7]. Sihvola and Kong presented an explicit formula for the effective permittivity [11]. They gave their formula for an arbitrary distribution of the NRs and used a dyadic notation which is not accessible for most nowadays readers. I will follow their method but I will use matrix notation, namely rotation matrices for the coordinate system, as will be explained immediately. In Eq. (2.9) I presented the effective permittivity for a composite of a nematic array of NRs. This equation can be presented as a function of the single NR polarizability:

$$\varepsilon_{eff}^{j} = \varepsilon_h + \frac{\varepsilon_h p \cdot \left(\alpha^j / V \right)}{\varepsilon_h - p \cdot L^j \left(\alpha^j / V \right)} \tag{6.1}$$

where α^j / V is the single NR polarizability normalized by the volume. For a composite with a certain angular distribution function, the polarizability in Eq. (6.1) should be replaced by a weighted averaging on the different NRs with their different orientation. A single NR in the array will have a certain orientation with tilt angle θ about the $\hat{z}$ axis and azimuthal angle φ relative to the $\hat{x}$ axis. The averaging is made using both θ and φ (see section 2.1.2 for the definition of the angles). The distribution for φ is a uniform distribution (random orientation) and the distribution for θ is the ADF presented in section 5.3. I will use the notation of triangle brackets for an averaging and a subscript to indicate over which angles the averaging is performed. An averaging of a general function $\psi(\Omega)$ (Ω is a solid angle) over the entire angular space is:

$$\langle\psi\rangle_{\theta,\varphi} = \int_0^{\pi} d\theta \cdot \sin\theta \cdot ADF(\theta) \int_0^{2\pi} \frac{d\varphi}{2\pi} \cdot \psi(\theta,\varphi) \tag{6.2}$$

The single NR polarizability and depolarization factor are second rank tensors, i.e [3×3] matrix, which in the local coordinate system of the NR are diagonal:

$$\overleftrightarrow{\alpha}_{NR} = \begin{pmatrix} \alpha_{\perp} & 0 & 0 \\ 0 & \alpha_{\perp} & 0 \\ 0 & 0 & \alpha_{\parallel} \end{pmatrix} \tag{6.3}$$

$$\overleftrightarrow{L}_{NR} = \begin{pmatrix} L_{\perp} & 0 & 0 \\ 0 & L_{\perp} & 0 \\ 0 & 0 & L_{\parallel} \end{pmatrix} \tag{6.4}$$

The subscript "*NR*" indicates the local coordinate system of the NR. I rotate the global coordinate system to the local coordinate system of the NR, apply the relevant tensors (see Eq. (6.1)) and rotate the result back to the global coordinate system. A rotation in φ around the $\hat{z}$ axis is:

$$\hat{R}_z(\varphi) = \begin{pmatrix} \cos(\varphi) & \sin(\varphi) & 0 \\ \sin(-\varphi) & \cos(\varphi) & 0 \\ 0 & 0 & 1 \end{pmatrix} \tag{6.5}$$

and a tilt in θ around the $\hat{y}$ axis is:

$$\hat{R}_y(\theta) = \begin{pmatrix} \cos(\theta) & 0 & \sin(-\theta) \\ 0 & 1 & 0 \\ \sin(\theta) & 0 & \cos(\theta) \end{pmatrix} \tag{6.6}$$

Treating the polarizability and depolarization factor as operators, the presentation of a general operator $\overleftrightarrow{A}_{NR}$ in the global coordinate system will be:

$$\overleftrightarrow{A}_{xyz}\left(\varphi,\theta\right)=\hat{R}_z\left(-\varphi\right)\hat{R}_y\left(-\theta\right)\overleftrightarrow{A}_{NR}\hat{R}_y\left(\theta\right)\hat{R}_z\left(\varphi\right) \tag{6.7}$$

The average effective permittivity will be:

$$\overline{\overleftrightarrow{\varepsilon}_{eff}}=\varepsilon_h\cdot\overleftrightarrow{I}+\varepsilon_h\frac{p\cdot\left\langle\overleftrightarrow{\alpha}_{xyz}\middle/V\right\rangle_{\theta,\varphi}}{\varepsilon_h\cdot\overleftrightarrow{I}-p\cdot\left\langle\left(\overleftrightarrow{L}\cdot\overleftrightarrow{\alpha}\right)_{xyz}\middle/V\right\rangle_{\theta,\varphi}} \tag{6.8}$$

where in places the host permittivity ε_h, appeared "alone" in Eq. (6.1), it was multiplied by unit matrix $\overleftrightarrow{I}$, which means I treat the host as an isotropic material. The result is a general [3×3] matrix, where no element in it is by definition zero. Nevertheless, after averaging over φ the result becomes a diagonal matrix with two identical elements (the elements correspond to ε_{xx} and ε_{yy}) and one independent element (ε_{zz}). This is because of the symmetry of the NRs in the two SAs and the uniform angular distribution over φ. The results are:

$$\overline{\varepsilon_{eff}^{x,y}}=\varepsilon_h+\varepsilon_h\frac{p\cdot\left\langle\alpha_{\parallel}\sin^2\theta+\alpha_{\perp}\left[2-\sin^2\theta\right]\right\rangle_{\theta}\middle/2V}{\varepsilon_h-p\cdot\left\langle L_{\parallel}\alpha_{\parallel}\cos^2\theta+L_{\perp}\alpha_{\perp}\left[2-\sin^2\theta\right]\right\rangle_{\theta}\middle/2V} \tag{6.9a}$$

$$\overline{\varepsilon_{eff}^{z}}=\varepsilon_h+\varepsilon_h\frac{p\cdot\left\langle\alpha_{\parallel}\cos^2\theta+\alpha_{\perp}\sin^2\theta\right\rangle_{\theta}\middle/V}{\varepsilon_h-p\cdot\left\langle L_{\parallel}\alpha_{\parallel}\cos^2\theta+L_{\perp}\alpha_{\perp}\sin^2\theta\right\rangle_{\theta}\middle/V} \tag{6.9b}$$

where we still need to weigh the value by $ADF\left(\theta\right)$. The behavior of the composite is like a uniaxial crystal that has one extraordinary refraction index in one direction (LA) and two ordinary refraction indices in the two other directions (SAs). All phenomena and application related to birefringence can be seen in such a composite.

If we would use $ADF\left(\theta\right)=\delta\left(\theta\right)$ the result would be that of a nematic array (Eq. (2.9)) and if we would use $ADF\left(\theta\right)=1/2$ the result would be that of random orientation that is isotropic:

$$\overline{\varepsilon_{eff}^{x,y}}=\overline{\varepsilon_{eff}^{z}}=\varepsilon_h+\varepsilon_h\frac{p\cdot\left(2\alpha_{\perp}+\alpha_{\parallel}\right)\middle/3V}{\varepsilon_h-p\cdot\left(2L_{\perp}\alpha_{\perp}+L_{\parallel}\alpha_{\parallel}\right)\middle/3V} \tag{6.10}$$

The result presented in Eq. (6.10) coincide with the theoretical expression for random orientation [7,8,11].

6.1.2 The nonlinear response – third order nonlinear susceptibility

$\chi^{(3)}$ is a forth rank tensor ($\chi^{(3)}_{ijkl}$), which in the general case can be presented as a matrix with 3^4=81 elements. It is well known that for all the 32 crystallographic point groups, the number of independent elements is much smaller and depends on the specific point group symmetry in question (see e.g. [16,33]). Yang and Xie presented a contracted approach to rearrange the independent elements of $\chi^{(3)}_{ijkl}$ into [3×10] matrices $\chi^{(3)}_{i,m}$ for all 32 crystallographic point groups [33]. When the NL interaction is made with one interacting field (e.g third harmonic generation and self phase modulation) in a certain linear polarization, oriented to crystallographic axis, the third order NL susceptibility can be presented with a scalar value $\chi^{(3)}_{eff}$ [16,33]. In the Kerr effect for example, the effective susceptibility is used in the calculations of the second-order nonlinear refractive index n_2 [34]. In all further analysis I will use this scalar effective susceptibility. Given the scalar third order susceptibility, the effective third order susceptibility of a nematic array will be a second order tensor, on account of the geometry of the NR (as the permittivity). Eq. (2.10) that describes the composite effective susceptibility can be written in terms of the second order hyperpolarizability (Eq. (2.7)):

$$\overleftrightarrow{\chi}^{(3)}_{eff} = p\,\overleftrightarrow{\gamma}\big/\left(\varepsilon_0 V\right) \qquad (6.11)$$

where the second order hyperpolarizability as an operator or a matrix is:

$$\overleftrightarrow{\gamma} = V\left(\frac{\varepsilon_h}{\varepsilon_h\cdot\overleftrightarrow{I}+\left(\varepsilon_i-\varepsilon_h\right)\overleftrightarrow{L}}\right)^4\varepsilon_0\chi^{(3)} \qquad (6.12)$$

The same analysis done for the effective permittivity (section 6.1.1) can be made here, by addressing $\overleftrightarrow{\gamma}$ as an operator in the local coordinate system of the NR, presenting it in the global coordinate system and averaging it with the ADF. Again the result is a [3×3] matrix that after integrating over φ becomes diagonal. The resulting independent elements, before the integration over θ are:

$$\overline{\chi_{eff}^{(3),x,y}} = p \cdot \left\langle 0.5 \cdot \left(f^{z}\right)^{4} \cdot \sin^{2}\theta + \left(f^{x,y}\right)^{4} \cdot \left(1 - 0.5 \cdot \sin^{2}\theta\right) \right\rangle_{\theta} \chi_{i}^{(3)} \tag{6.13a}$$

$$\overline{\chi_{eff}^{(3),z}} = p \cdot \left\langle \left(f^{x,y}\right)^{4} \cdot \sin^{2}\theta + \left(f^{z}\right)^{4} \cdot \cos^{2}\theta \right\rangle_{\theta} \chi_{i}^{(3)} \tag{6.13b}$$

where I define $f^{j} = \frac{\varepsilon_h}{\varepsilon_h + L^{j}\left(\varepsilon_i - \varepsilon_h\right)}$. Again, using $ADF\left(\theta\right) = \delta\left(\theta\right)$ will result with Eq. (2.10) and using $ADF(\theta) = 1/2$ will result with random orientation composite that is isotropic:

$$\overline{\chi_{eff}^{(3),x,y}} = \overline{\chi_{eff}^{(3),z}} = p \cdot \left[2\left(f^{x,y}\right)^{4} + \left(f^{z}\right)^{4}\right] \chi_{i}^{(3)} \Big/ 3 \tag{6.14}$$

It is important to notice that we assume in all the derivations that the inclusions alone contribute to the nonlinearity (the polymer host has negligible NL susceptibility). In addition, the assumptions made to use a scalar value for $\chi_{eff}^{(3)}$ were made for simplicity. The basic concepts of the model presented here are applicable also for the full tensorial susceptibility, given the whole tensor is known.

6.2 Results and analysis

In this section I will examine the influence of different parameters on the results of the composite effective permittivity and third order NL susceptibility. The results are of Eqs. (6.9a-b) and (6.13a-b) for the permittivity and third order susceptibility, respectively. I used again PFCB as the host and CdSe as the NRs. I will start from examining the influence of the capsule shape analysis on the results. I will then examine the influence of the dimension of the single NR – volume and AR, and I will finish with the influence of the temperature. For the capsule shape analysis, I will present the results for both the composite effective permittivity and third order susceptibility. For the other parameters, I will present the result for the third order susceptibility alone. The results are analyzed for different alignment degree, from random orientation through partially aligned array (with different aligning field strengths) to nematic array.

6.2.1 Influence of the capsule shape analysis

I used as an example the first NR dimensions presented in Table 3 (60×3.1nm, see section 5.2). I used the bulk properties of the NR material despite the small radius, which will cause quantum confinement effects. For the calculations of the permittivity and third order susceptibility I used the properties for optical frequencies. For the calculation of the alignment mechanism and the ADF I used the properties for DC electric fields.

The values used are: volume fraction – $p = 4\%$, permittivity for DC (or low frequencies) electric fields: $\varepsilon_{CdSe,\|} = 10.2$, $\varepsilon_{CdSe,\perp} = 9.33$, $\varepsilon_{PFCB} = 2.4$, permittivity for optical frequencies: $\varepsilon_{CdSe,\|} = \varepsilon_{CdSe,\perp} = 6.2$, $\varepsilon_{PFCB} = 2.19$.

For the comparison between the prolate spheroids and the capsule shapes, the value of the depolarization factor of the capsule shape was taken as the effective value, as explained in section 4.3. The values of the PDM of the capsule shapes were taken as explained in section 5.2. The values for the ellipsoid PDM were calculated from the data of Li and Alivisatos [25], treating the NRs as prolate spheroids, but with the formula given by Sihvola for the polarizability (see section 2.1 and Appendix A).

Table 4. Effective permittivity ε_{eff} and third order NL susceptibility normalized by the inclusions susceptibility $\chi^{(3)}_{eff} \big/ \chi^{(3)}_{CdSe}$ in the parallel direction, for NR dimension 60×3.1nm $p = 4\%$. Comparison between prolate spheroid and capsule shape models, with and without PDM.

E0 [V/m]	ε_{eff}				$\chi^{(3)}_{eff} \big/ \chi^{(3)}_{CdSe}$			
	Without PDM		With PDM		Without PDM		With PDM	
	Prolate spheroids	Capsule shapes	Prolate spheroids	Capsule shapes	Prolate spheroids	Capsule shapes	Prolate spheroids	Capsule shapes
0 (random)	2.3006	2.3002	2.3006	2.3002	1.47%	1.39%	1.47%	1.39%
10^6	2.3006	2.3002	2.3007	2.3002	1.47%	1.39%	1.47%	1.39%
$5 \cdot 10^6$	2.3007	2.3006	2.3019	2.3022	1.47%	1.41%	1.53%	1.48%
10^7	2.3009	2.3021	2.3053	2.3076	1.48%	1.48%	1.69%	1.74%
$5 \cdot 10^7$	2.3084	2.3364	2.3330	2.3401	1.84%	3.08%	3.03%	3.26%
10^8	2.3296	2.3440	2.3421	2.3445	2.86%	3.44%	3.47%	3.47%
∞ (nematic)	2.3488	2.3463	2.3488	2.3463	3.80%	3.55%	3.80%	3.55%

Effective permittivity:

The result for a composite with sphere inclusions, with the same volume fraction, is $\varepsilon_{eff} = 2.2915$, orientation independent. NR composite presents larger values from that of sphere inclusions, even for random orientation (enhancement of 0.4% and 0.38% for spheroids and capsule shapes, respectively), which coincide with theoretical prediction (see Eq. (6.10)). The reason is that each component of the polarizability (each direction) contributes one third of its value to the general polarizability. The sphere polarizability is replaced by an average of the three components, which is larger than the result for a sphere (see Eq. (6.10) and [7]). Regarding the two orientation extremes (random and nematic), it can be seen that the capsule shape values are smaller than those of the prolate spheroid. This is due to the larger depolarization factor of the capsule shapes, as explained in section 4.3. For a partially aligned composite, without PDM presence, starting from aligning field of 10^7V/m the capsule shape larger volume start to affect the alignment (see section 4.2), hence the composite values are higher. With the presence of the PDM, the alignment starts to affect from aligning field of $5 \cdot 10^6$ V/m.

Effective third order NL susceptibility:

For the Effective third order NL susceptibility, I present the results normalized by the inclusions susceptibility $\chi^{(3)}_{eff} \big/ \chi^{(3)}_{CdSe}$. The result for sphere inclusion composite is $\chi^{(3)}_{eff} \big/ \chi^{(3)}_{CdSe} = 0.61\%$. Here the difference between the sphere inclusion and random NR composite is much larger (enhancement of 144% and 132% for spheroids and capsule shapes, respectively). The reason is that in the expression for the susceptibility of a random composite (Eq. (6.14)), the term consisting the depolarization factor (which is the geometrical description) is raised to the power of four, which makes the geometry influence very strong. The general behavior of the effective susceptibility is the same as with the permittivity. Here for aligning field of $5 \cdot 10^7$V/m, the alignment effect is substantial and there is 7.68% enhancement due to the presence of the PDM and more than 130% enhancement relative to the random orientation result.

6.2.2 Dimension dependency

In this section, I examine the influence of the shape of the single NR in the composite, on the average macroscopic characteristics. I will focus on the third order NL susceptibility and will separate this section into two topics:

(a) The dependency on the volume.

(b) The dependency on the axes AR.

As explained (section 5.3) the volume of the single NR affects only the alignment mechanism, by enhancing both the induced and permanent dipole moments, which in turn makes the alignment stronger. The axes AR, on the other hand, affect both the result for a nematic array and the induced dipole moment (by the influence on the single NR polarizability). Both of the effects favor larger AR.

(a) Macroscopic characteristics dependency in the single NR volume:

In order to examine the influence of the single NR volume on the alignment and hence the macroscopic characteristics in interest ($\chi_{eff}^{(3)}$) I will use equal AR NRs (capsule shapes) with different volumes. As explained (section 3.3) the minimum width of the capsule shape, determined by two times the Bohr radius of the bulk exciton, is set on $12nm$. I will use an AR of 10, and use depolarization factor of $L^{LA} = 0.0305$ (see Table 2 at section 4.3) and therefore $L^{SA} = 0.5\left(1 - L^{LA}\right) = 0.4848$, for different volume NRs. For the PDM, I will use a permanent polarization density of 0.205 μC/cm^2 (see section 5.2). The volume fraction was set on $p = 4\%$, and since it was kept constant, the results for the random orientation and nematic array composite were not affected by the change of the single NR volume. In Fig. 14, I present the result for four different NRs (same AR, different volume). I examine the change in the effective susceptibility as a function of the aligning field strength. The NRs dimensions presented in the figure:

$L\ [nm]$	$W\ [nm]$	AR	$V\ [nm^3]$
180	18	10	44,278
160	16	10	31,098
140	14	10	20,833
120	12	10	13,119

In order to compare different NRs, I need to define a "measurement tool" .I define $\bar{E}$ as the aligning field strength needed, to bring the effective susceptibility half the way between the value of a random-orientation composite and a nematic-array composite. A composite which requires a small $\bar{E}$, can be treated as a "better" composite, because less effort is needed to achieve the same resulted susceptibility. From Fig. 14 it can be seen that composite with larger volume NRs, needs smaller $\bar{E}$.

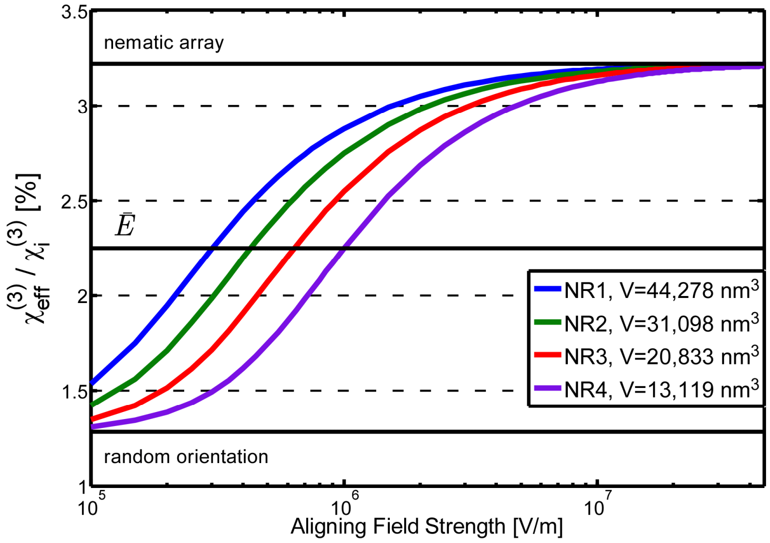

Fig. 14: Dependency of the composite effective third order NL susceptibility (normalized by the inclusions' susceptibility) on the single NR volume. Equal AR of 10. Presented also the values for the random orientation and nematic array composites and the "half way" value.

As explained, the single NR volume does not affect the results for the random orientation and nematic array composites. All four curves originate and converge at the same points. However, increasing the volume of the single NR from ~13,100 nm^3 to ~44,200 nm^3, reduces the field strength required, $\bar{E}$, from 1×10^6 V/m to 3×10^5V/m, about 3 times smaller. In Fig. 15.a, 15.b and 15.c, I present the dependency of the required field strength $\bar{E}$ on the single NR volume for AR=5,10,20, respectively. The LA depolarization factors were changed accordingly for each AR: 0.0648, 0.0305, 0.0147, respectively.

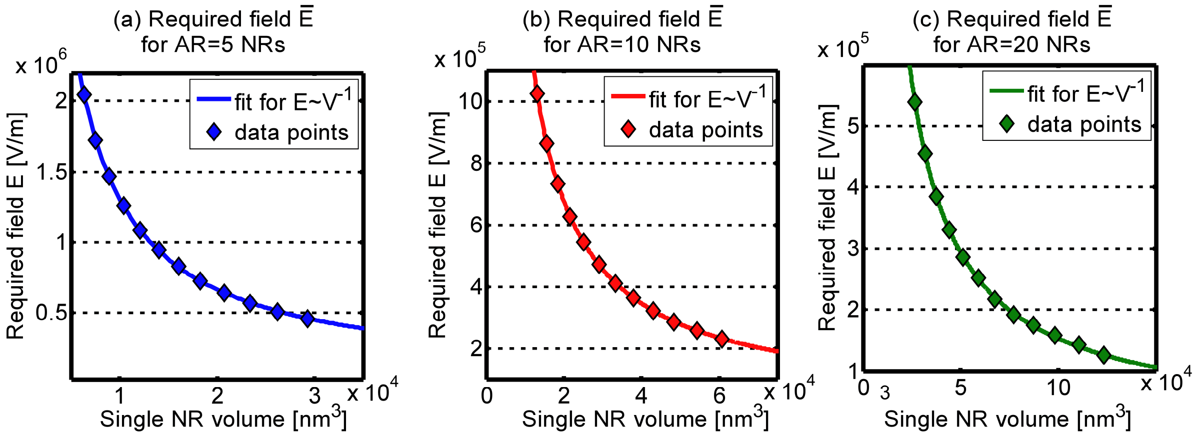

Fig. 16: Dependency of required aligning field strength $\bar{E}$ on the single NR volume with the same AR. Data points and fit curves for $\bar{E} \sim V^{-1}$. (a) AR=5. (b) AR=10. (c) AR=20

As can be seen from the figure, the required field strength falls like one over the single NR volume. I fitted the data sets to the equation $A \cdot V^{-1} + B$ when A, B are unknown parameters. The resulted equations are:

$$\bar{E}_{AR=5} = 1.29 \cdot 10^{10} \cdot V^{-1} + 2260 \text{ , } \bar{E}_{AR=10} = 1.31 \cdot 10^{10} \cdot V^{-1} + 7670 \text{ , } \bar{E}_{AR=20} = 1.33 \cdot 10^{10} \cdot V^{-1} + 1850$$

It can be seen that changing the AR, does not affect the results substantially – the parameter A changes by 3% when increasing the AR from 5 to 20 (4 times larger). The meaning of the similarity of the results is that the AR does not have a significant role in the alignment mechanism. In the next section I will examine the dependency in the AR more deeply.

(b) Macroscopic characteristics dependency in the single NR AR:

For the dependency in the AR, I set the volume on a constant value and change the AR. The NRs dimensions I use:[3]

L [nm]	W [nm]	AR	V [nm^3]
100	20	5	30,000
158	15	10	30,000
206	13	15	30,000
249	12	20	30,000

Again I present the results of the effective third order NL susceptibility, normalized by that of the inclusions (Fig 16).

---

[3] These are rounded numbers, hence the length divided by the width does not equal the AR exactly. In addition, I ignored here the upper limit length mentioned in section 3.1.1

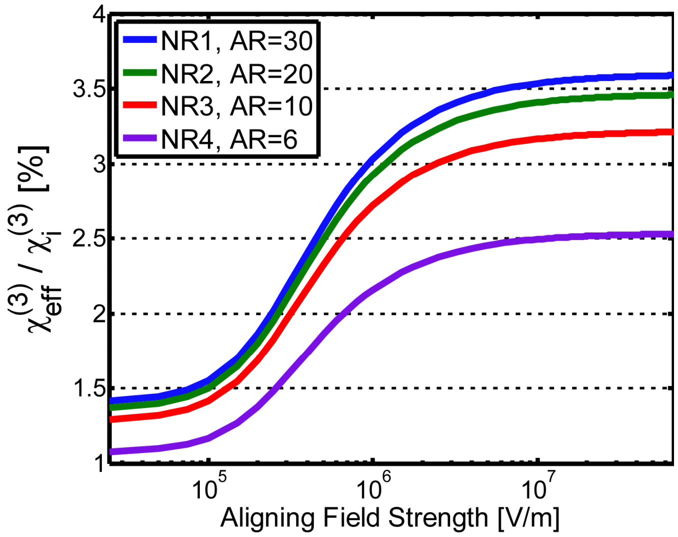

Fig. 16: Dependency of the composite effective third order susceptibility (normalized by the inclusions' susceptibility) on the single NR AR. Equal volume of 18,500 nm^3.

For the case of different AR NR, the values for random orientation and nematic array composite differ with the AR. This can be seen from the equations (nematic array – Eq. (2.10), random orientation – Eq. (6.14)) and in Fig. 16; each curve originates and converges in different points. This is in contrast to Fig. 15 where all the curves start and end at the same points. From Fig. 16 I can extract the difference in the values for the random orientation and nematic array composites. Increasing the AR from 6 to 30, increases the value for random orientation composite, from 1.18% to 1.51%. The value for a nematic array composite, increases from 2.73% to 3.75%.

In order to use the "half way" aligning field strength, to compare between the different composites, I normalized the four curves: for each curve I set the random orientation value (starting point) to zero and normalized the curve by its nematic array value.

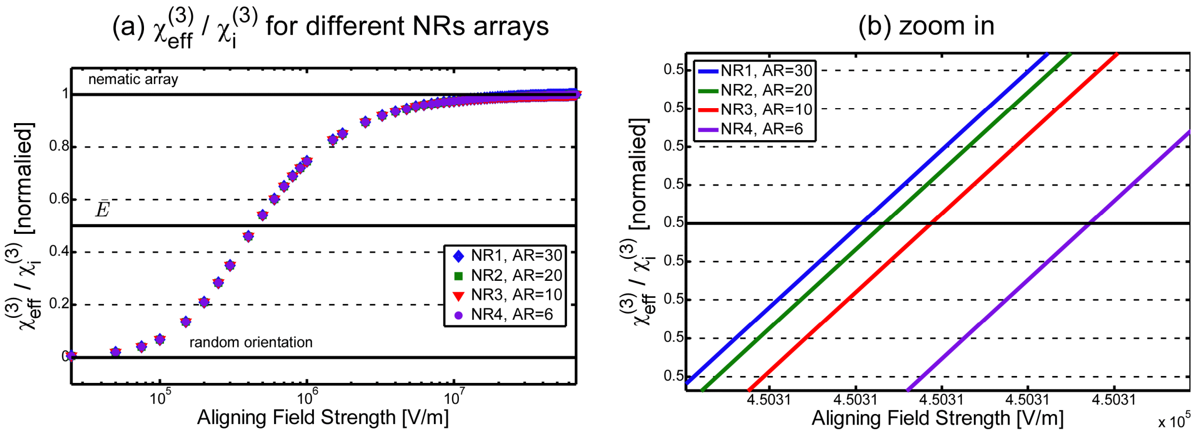

Fig. 17: (a) Dependency of the composite effective third order susceptibility (normalized by the inclusions' susceptibility) on the single NR AR. Results are normalized to the same starting point (0) and same ending point (1). (b) Zoom in to observe the differences between the different composites

As can be seen from Fig. 17.a, the influence of the AR on the alignment is very small. The different curves are almost indistinguishable. I used discrete markers so the different data sets will be visible. In Fig. 17.b I present a zoom in (with solid lines) and the differences between the curves are visible. Larger AR NR, has smaller required aligning field $\bar{E}$, but the differences are negligible.

6.2.3 Temperature dependency

The last parameter I wish to examine is the temperature. As explained, PFCB polymerization temperature is 120-350°C, where higher temperature needs shorter polymerization time [31]. Nanocrystals, on the other hand, may become unstable at elevated temperature (see e.g. [35] for influence of temperature on nanocrystals). For the calculations so far, I assumed a temperature of 150°C and examined also the influence of a decreased temperature of 120°C on the ADF (see section 5.3). The choice in 150°C, evolved from the conjecture that this is a temperature that the NRs will still be stable in, when further investigation is needed to explore the exact temperature limit. In this section I will examine the influence of the temperature on the NL susceptibility, in the range of 100-200°C. I will compare again the field strength required to bring the effective susceptibility to half the way towards the nematic value, $\bar{E}$. I simulated a single NR, with the dimensions:

$L\ [nm]$	$W\ [nm]$	AR	$V\ [nm^3]$
120	12	10	13,119

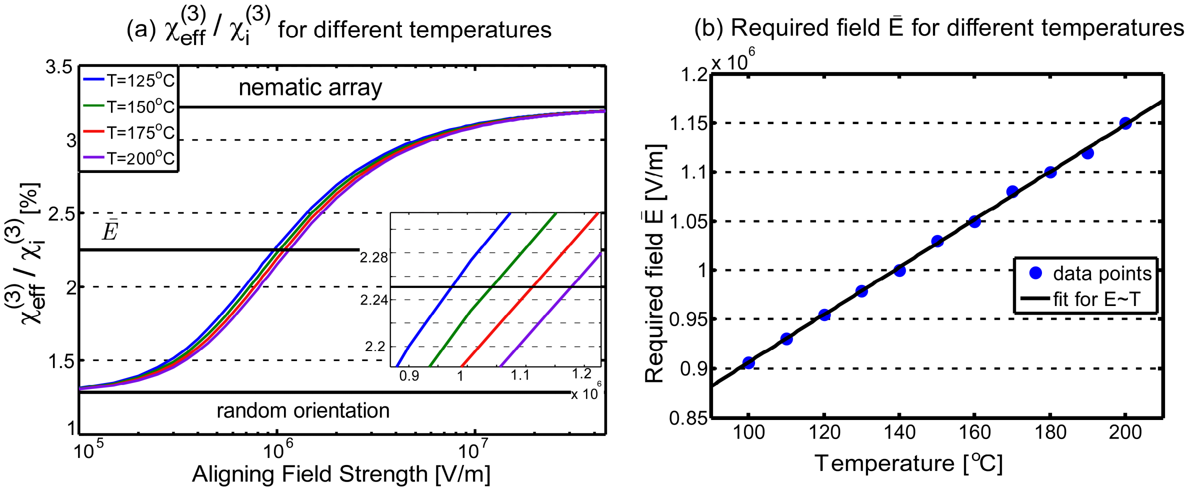

Fig. 18: (a) Dependency of the composite effective third order NL susceptibility (normalized by the inclusions' susceptibility) on temperature. Inset – zoom in. (b) dependency of the required field strength on the temperature, with a linear fit curve.

Fig. 18.a presents the change in the relative susceptibility, at four different temperatures. Here the random orientation (starting point) and nematic array values are the same for all four curves, since they represent the same NRs composite. The curves of lower temperatures are higher for all aligning field strengths, as expected, since the thermal fluctuations of the NRs orientation are smaller. In addition, they cross the line of the half way between the random orientation and nematic array values, at lower aligning field strength, as expected. Decreasing the temperature from 200°C to 125°C, reduce the aligning field strength required, $\bar{E}$, from 1.8×10^6 V/m to 9.7×10^5V/m, 46% less. Fig. 18.b presents the dependency of the aligning field strength required, $\bar{E}$, in the temperature, and a linear correlation is observed.

7. Nonlinear waveguides

All of the former sections dealt with the characterization of the PFCB-CdSe NRs composite as a NL material. The macroscopic characteristics of the composite in interest were the permittivity and especially the third order NL susceptibility. As explained in the introduction, the main goal of the research is to fabricate a NL WG, using the NL composite as the core. In this section, I wish to characterize the WG that will be fabricated using the composite. The cladding of the WG planned is made of Cytop which is a commercially polymer with low losses and low refractive index (1.34) for 1.55µm wavelength. I will start from two basic concepts in NL WGs, without addressing the whole theoretical background for WGs and NL WGs.

7.1 Waveguide design

The basic idea of a WG is to confine the propagating wave in the core of the WG. This is done by using higher refractive index material for the core and lower refractive index material for the clading (see e.g. [34]). In Fig. 19.a, I illustrate the WG in 3D, where the propagation direction is set as the $\hat{z}$ axis. The alignment mechanism will be done by two electrodes, parallel to the WG core, on both its sides, that will apply the aligning field (Fig. 19.b and 19.c). The applied field will be along the $\hat{x}$ axis, hence the NRs LA will be directed in the $\hat{x}$ axis direction and this will be the notation from now on. If the electrodes will be too close, the optical mode will be truncated by the metal electrodes (Fig. 19.d), which will cause significant loss. Our simulations show that a distance of 3.5 µm between the WG core and the electrodes will make this loss to be negligible (Fig. 19.e). In the next section I will examine also the optimization of the core dimensions.

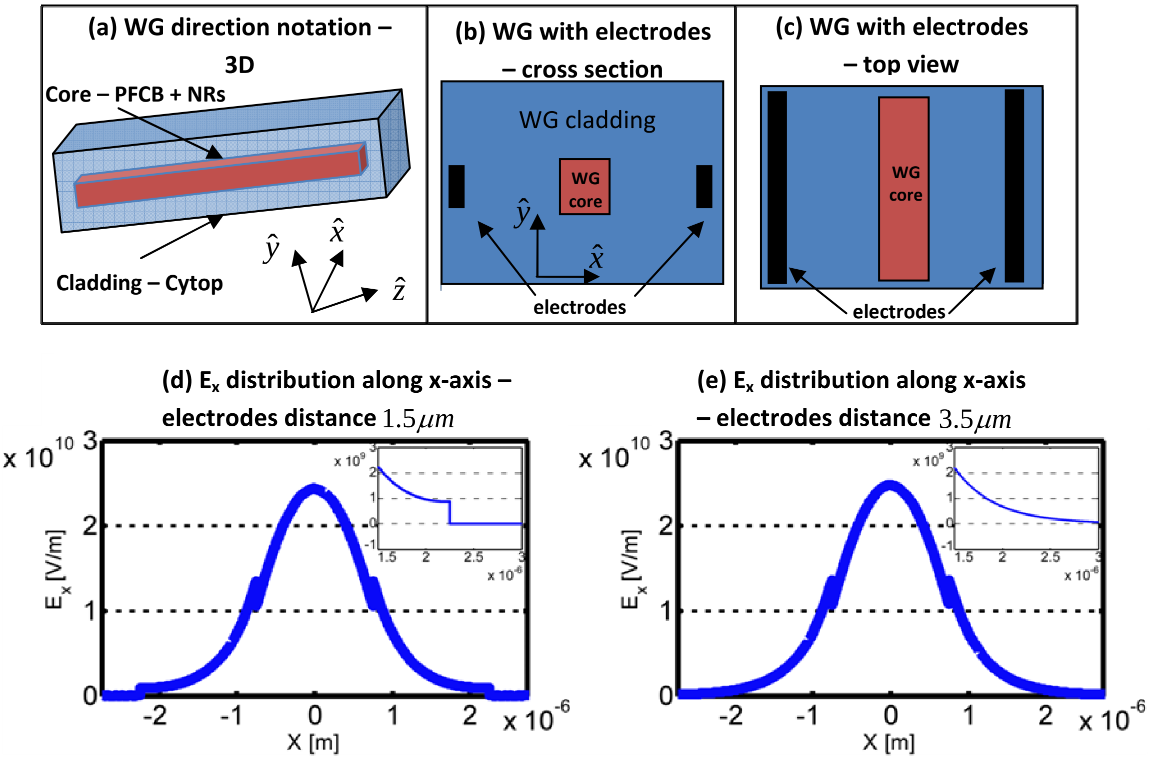

Fig. 19: (a) WG illustration in 3D with the direction notation. (b) WG cross section with the electrodes location. (c) The same from top-view. (d) Optical electric field distribution along the $\hat{x}$ axis (through the center of the core) with electrodes distance of 1.5 µm from the core. Inset – zoom in for the truncation of the field. (e) Same as (d) for distance of 3.5 µm, no truncation.

7.2 Effective modal area in waveguides

The measure for the quality of the confinement of the mode, in NL WGs, is the "effective modal area", A_{eff}. I present the notation for A_{eff}, given by Koos *et al.* for high index contrast WGs [21]:

$$A_{eff} = \frac{Z_0^2}{n_{core}^2} \frac{\left| \int\limits_{A_\infty} \mathrm{Re}\left\{ \vec{E}(x,y) \times \vec{H}^*(x,y) \right\} \vec{e}_z \, dA \right|^2}{\int\limits_{A_{core}} \left| \vec{E}(x,y) \right|^4 dA} \tag{7.1}$$

where $\vec{e}_z$ is a unit vector in the $\hat{z}$ direction (see Fig. 19.a for direction notation) $Z_0 = \sqrt{\mu_0/\varepsilon_0} = 377\Omega$ is the free-space wave impedance and n_{core} is the refractive index of the WG core material, which is a diagonal matrix in my case. The integrations in Eq. (7.1) are surface integrations on the cross section of the WG. The integration in the numerator is on the entire cross section – core and cladding, assuming the cladding is infinite. The integration in the denominator is on the cross section of the core only, where the NL interaction ocurs.

I will examine the influence of the dimensions of the core of the WG ion the effective modal area. I will start from examining a rectangle core shape WG. Former work done in our lab aimed at fabrication of a square WG, with dimensions of 1.5×1.5μm^2 [13,14]. I will examine different AR rectangle WGs, around this shape, looking for the smallest effective modal area. Afterwards, I will examine different dimensions of square WGs. For the simulation of the effective modal area, the NL susceptibility is not used (see Eq. (7.1)).

I use a composite with NRs dimension of 12×120nm (W×L), polymerization temperature of T=150^{o}C and volume fraction of $p = 4\%$. For this composite the required aligning field strength $\bar{E}$ (as defined in section 6.2), is 10^6 V/m, which results with permittivity along the LA of $\varepsilon_{eff}^{LA} = 2.3210$ $\left(n^{LA} = 1.5235\right)$ and along the SA $\varepsilon_{eff}^{SA} = 2.2881$ $\left(n^{SA} = 1.5126\right)$. The calculation of A_{eff} was done by simulating the WG with specific refractive indices (a diagonal 3×3 matrix) and integrating the expressions in Eq. (7.1), all using COMSOL Multiphysics.

In Fig. 20, I present typical results of the simulation (presenting the normal value of the electric field for a 1.5×1.5μm^2 core WG). The results are along the $\hat{x}$ axis (through the core center), for an optical field ploarized along the $\hat{x}$ axis (Fig. 20.a) and along the $\hat{y}$ axis (Fig. 20.b). The integration in the numerator of Eq. (7.1) is over the whole cross section plane. In my case, I set the integration on a cross section of 20×20μm^2. The value of the field in the center of the WG core in the simulations is ~3×10^{10}V/m, while the value of the field in the ending of the clad is 46V/m for polarization in the $\hat{x}$ direction and 0.07V/m for polarization in the $\hat{y}$ direction, which means I can neglect the field outside of the clad region and treat it as zero.

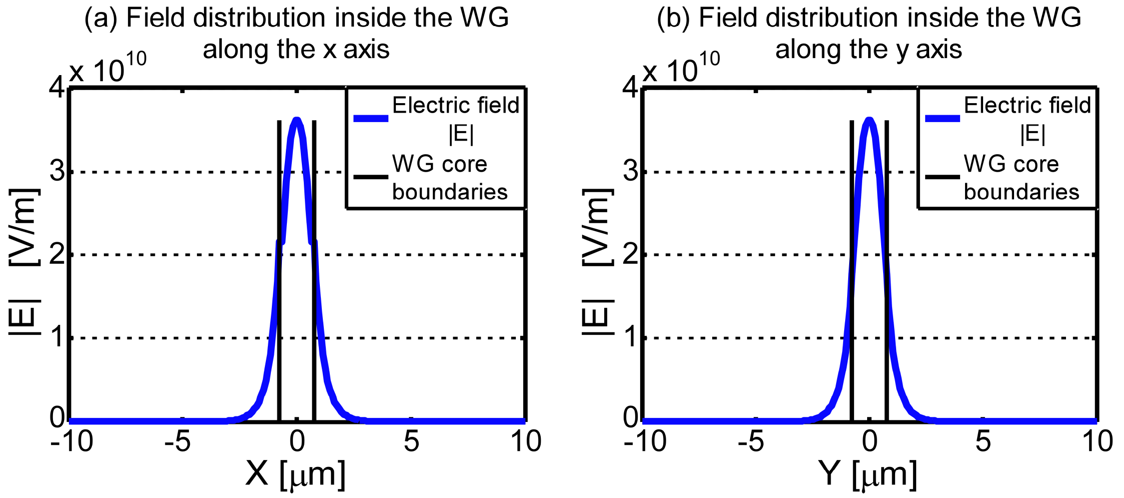

Fig. 20: Simulation results of the optical electric field $|E|$ in the WG. (a) Along the $\hat{x}$ axis through the center of the core. (b) Along the $\hat{y}$ axis through the center of the core.

The differences between polarization of the optical field along the $\hat{x}$ and $\hat{y}$ axes are negligible, regarding A_{eff}. For the rest of this section I will present results only for the electric field polarized along the $\hat{x}$ axis. In Fig. 21.a, I present the results for the different effective modal area for different rectangle WGs. The results are presented as a function of the AR which is defined here as $AR = L_x / L_y$ where L_x, L_y are the WG core dimensions along the $\hat{x}$ and $\hat{y}$ axes, respectively. The minimal effective area is with AR=1 – meaning a square WG. For a square WG the minimum effective area is obtained for $1.3\times1.3\mu m^2$ core dimensions – 2.6 μm^2 (Fig. 21.b). As mentioned, former work done in our lab aimed at $1.5\times1.5\mu m^2$ core dimensions [13,14], resulting with – 2.7 μm^2 effective modal area (3.8% larger).

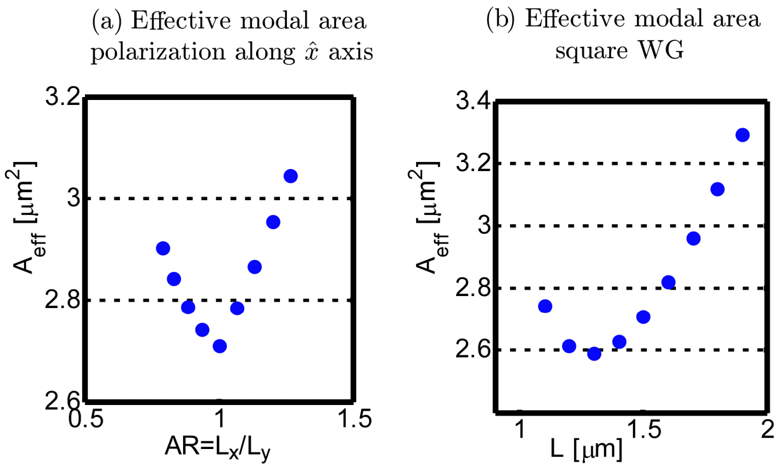
(a) Effective modal area polarization along $\hat{x}$ axis

(b) Effective modal area square WG

Fig. 21: Effective modal area results A_{eff} for: (a) Rectangular WG with different sides AR. Polarization along the $\hat{x}$ axis. (b) Same for square WG with different side lengths.

7.3 Nonlinear parameter of nonlinear waveguides

The characterization of the NL WG quality is the NL parameter, γ [21]:[4]

$$\gamma = \frac{3\omega \cdot \varepsilon_0 Z_0^2}{4n_{core}^2 A_{eff}} \chi^{(3)} \tag{7.2}$$

where ω is the optical frequency of the propagating wave. This parameter is used in the NL Schrödinger equation and describes the strength of the NL interaction in the NL WG. The two significant parameters in Eq. (7.2), that I am concerened with, are the effective modal area A_{eff} and the third order NL susceptibility $\chi^{(3)}$, which in my case will be the effective value of the PFCB-NRs composite. The dimension of the NL parameter is $(W \cdot m)^{-1}$. Common silica based NL optical fibers usually have NL parameter value of $\gamma = 1-3\times10^{-3}(W \cdot m)^{-1}$ [34]. Silica variant NL optical fibers have demonstrated relatively enhanced nonlinearity of $\gamma = 0.1-50(W \cdot m)^{-1}$ [36-39].

I will use the same composite parameters as in the former section: NRs dimension of 12×120nm (W×L), temperature of T=150°C and volume fraction of $p = 4\%$. The resulted

---

[4] The letter γ was used also to describe the second order NL hyperpolarizability. In all further analysis I will not use the hyperpolarizability and the letter γ will be used only for the NL parameter of the NL WG.

third order susceptibility are $\chi_{eff}^{(3)} / \chi_{CdSe}^{(3)} = 2.25\%$ along the LA and $\chi_{eff}^{(3)} / \chi_{CdSe}^{(3)} = 0.8\%$ along the SA. CdSe third order susceptibility is $\chi_{CdSe}^{(3)} = 3 \cdot 10^{-17}\, m^2/W$ [40]. In Fig. 22, I present the values of the refractive indices (Fig. 22.a) and NL parameters γ (Fig. 22.b) for two square WGs: 1.3×1.3µm^2 and 1.5×1.5µm^2. I compare for each one, different aligning field strengths, again for optical electric field polarized along the $\hat{x}$ (LA) direction. Regarding the refractive index, the results are the same for both WG core dimensions, since it is not influenced by the effective modal area. Regarding the NL parameter, the 1.3×1.3µm^2 core WG, present higher results. It can be seen from Fig. 22.b that the values for the 1.3×1.3µm^2 core WG are larger for all aligning field strengths. In contrast to the composite characteristics (presented in section 6.2), here the results for the random orientation (starting point of the curve) and nematic array (end point) are not the same.

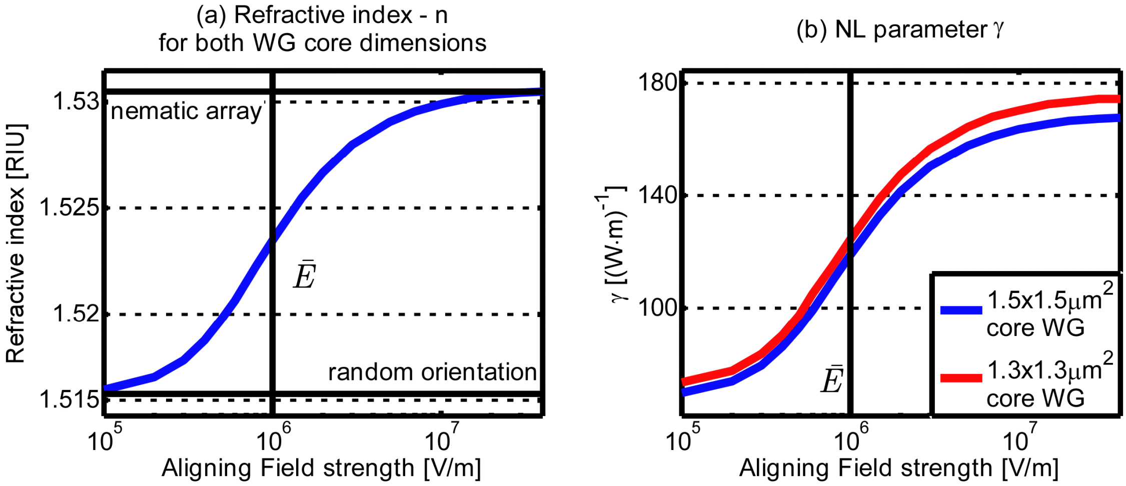

Fig. 22: Refractive index and NL parameter as a function of the aligning field strength. Optical electric field polarization along the $\hat{x}$ axis.
(a) – Refractive index n, for 1.5×1.5µm^2 and 1.3×1.3µm^2 core dimensions (same results). The values for random orientation, nematic array and "half way" aligning field between them also presented.
(b) – NL parameter γ, for 1.5×1.5µm^2 (blue) and for 1.3×1.3µm^2 (red) core dimensions.

For the aligning field strength required to bring the composite NL susceptibility, to half the value between random and nematic, $\bar{E}$, there is a small difference between the two WG core dimensions: $\gamma = 119 (W \cdot m)^{-1}$ for 1.5×1.5µm^2 core WG and $\gamma = 120.5 (W \cdot m)^{-1}$ for 1.3×1.3µm^2 core WG (1.2% improvement). The difference between the values for the nematic array is slightly larger: $\gamma = 168\left(W \cdot m\right)^{-1}$ for 1.5×1.5μm^2 core WG and $\gamma = 175\left(W \cdot m\right)^{-1}$ for 1.3×1.3μm^2 core WG (4.1% improvement).

It is worth noting, that for the 1.5×1.5μm^2 and electrodes distance from the core of 3.5μm each (see section 7.1), the total pitch between the two electrodes will be 9.5μm. Taking small fabrication errors, I will consider a pitch of 10μm. Applying a DC voltage of 100V will result with an aligning field of 10^7V/m. The issue of the dielectric strength (breakdown voltage) of the polymers was not addressed so far. The dielectric strength of the Cytop is 10^8V/m (manufacturer data). There is no data available for the PFCB dielectric strength. However polymers dielectric strength values are usually at the scale of ~10^8V/m [41], even for the unannealed polymers (the polymer in the liquid form). On the other hand, the fact that the aligning field is applied on the PFCB with NRs inside it and at elevated temperature has to be taken into account, as well. Experiments regarding the dielectric strength are planned in the near future. Nevertheless, aligning fields at the scale of ~10^7V/m, can be considered. For such an aligning field the resulted NL parameter for 1.5×1.5μm^2 core WG, is $\gamma = 164\left(W \cdot m\right)^{-1}$, very close to the nematic array value.

Another interesting characteristic to examine is the birefringence of the WG, which evolve of course from the birefringence of the composite itself. As explained, there is no difference between the two core dimensions regarding the refractive index. In Fig. 23 I show the birefringence $\Delta n = n_x - n_y$, again as a function of the aligning field strength. I show also the values for the random orientation $\left(\Delta n = 0\right)$ and for the nematic array $\left(\Delta n = \max\right)$. The value for the required field $\bar{E}$ is $\Delta n = 0.0108$.

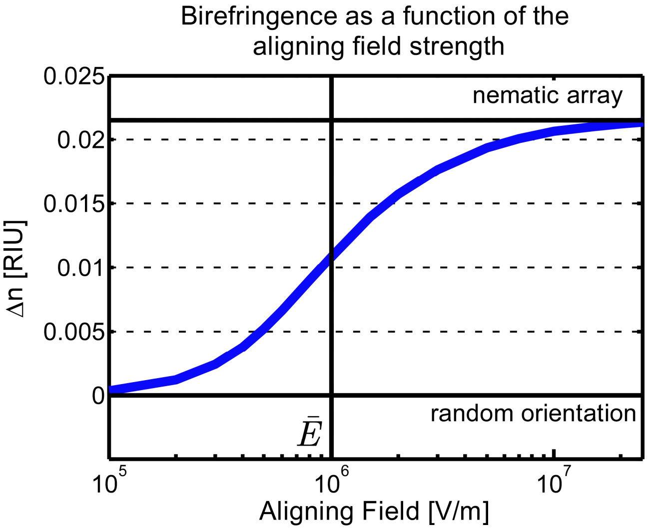

Fig. 23: Birefringence of the WG. The change in the birefringence as a function of the aligning field strength.

The last analysis I wish to present is a comparison between optical electric field polarization along the $\hat{x}$ and $\hat{y}$ axes, and refer also to a statistical analysis. All of the results for the composite permittivity and NL susceptibility used so far were the average or mean values (see section 6.1). The values of the refractive index and NL parameter, were also the values that were calculated from the average values of the composite. Here I wish to refer also to standard deviation (STD) of the results. The STD was calculated for the composite characteristics, permittivity and NL susceptibility, and from them the STD of the refractive index and NL parameter were derived. In Fig 24, I present the results for the refractive index (Fig 24.a) and NL parameter (Fig 24.b), for both polarization along the $\hat{x}$ direction (LA, blue line) and along the $\hat{y}$ direction (SA, red line), and the STD values. The results are for $1.5\times1.5\mu m^2$ core WG. The shaded areas are the mean values ±1STD. For small aligning field strengths there is an overlap between the two shaded areas, meaning there is a chance that the WG will behave the same for both polarizations. To avoid this chance, the aligning field strength should be above $\sim1\times10^6$ V/m.

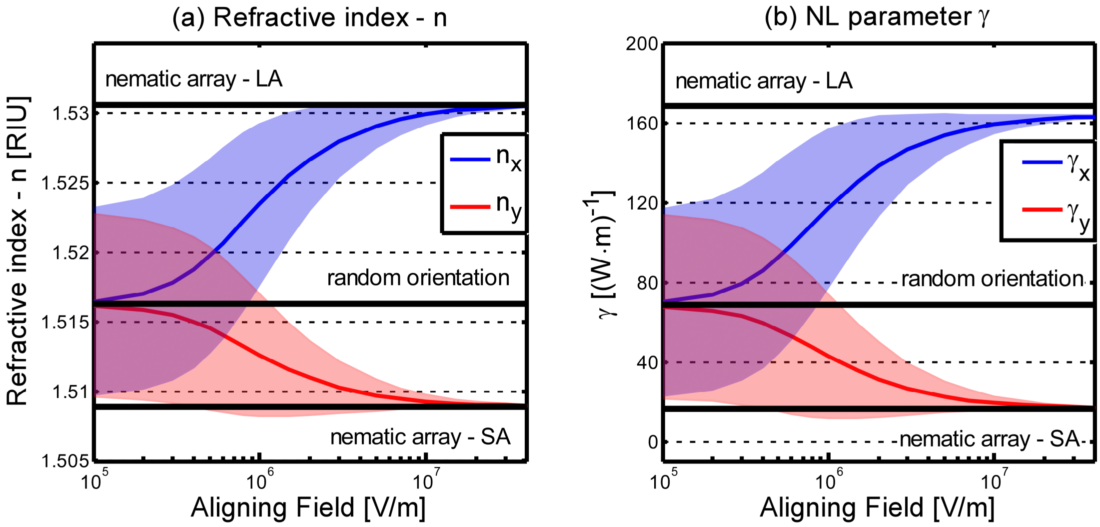

Fig. 24: Refractive index (a) and NL parameter (b) as a function of the aligning field strength, with the values for ±1 STD deviation. Optical electric field polarization along the $\hat{x}$ (blue) and $\hat{y}$ (red) axis are presented, with the values for random orientation and nematic array composites.

The results for the NL parameter γ are very high. As mentioned in the opening of this section, glasses based NL optical fibers achieve maximum values of $\gamma = 50(W \cdot m)^{-1}$. My results for the random orientation composite are $\gamma = 68(W \cdot m)^{-1}$, higher by 45% and this is the lower value. The alignment increases the results much more. Looking even at relatively low aligning field of 10^6V/m results with very high values of $\gamma = 119(W \cdot m)^{-1}$, for the LA direction. At that aligning field, the NL parameter for the SA direction is $\gamma = 42(W \cdot m)^{-1}$.

I will finish with mentioning that more work regarding dispersion engineering of the WG is needed in the future.

Summary

I started my work with theoretical background, describing the behavior of a single particle under a DC electric field. I described its linear response, i.e the polarizability and rotating moment and its NL response i.e the hyperpolarizability. I moved on to describe a composite with semiconductor NRs embedded in a dielectric host. The composite characteristics described were the permittivity and third order NL susceptibility, for a nematic array of NRs, meaning all the NRs are aligned at the same direction. I showed how NRs with large axes aspect-ratio result with larger permittivity and NL susceptibility.

After the relevant background, I explained the basic assumptions needed for my work:

(1) Electrostatic assumption for treating the composite as a homogeneous material.
(2) Optical assumption for the NL behavior in interest, i.e Kerr-type nonlinearities.
(3) Minimum NR size to avoid consideration of quantum-confinement effects.

After that, I explained why CdSe is the best choice for the NRs material, due to bandgap energy considerations. CdSe bandgap is slightly above the two photon energy for 1.55µm wavelength, which on one hand decays the two-photon-absorption process and on the other it is the optimize region for Kerr-type processes I am interested with.

I started the analysis of the composite, with the description of the NRs as capsule shapes, rather than the prolate spheroid shape usually used in theoretical work. I explained the geometry of the capsule shape and its electrostatic characteristics. I showed also how to use the simulation results of the capsule shapes, in order to find an equivalent prolate spheroid shape, which enables me to use this shape in analytical equations that were derived for prolate spheroids.

I proceeded with explanation of the alignment mechanism, with which the NRs will be aligned – a DC electric field, acting during the polymerization of the host PFCB polymer, which causes a rotating moment on the NRs. I showed how larger volume NRs and NRs with permanent-dipole-moment enhance the alignment process significantly. Finally, I calculated the angular-distribution-function of the NRs in the composite, with and without the permanent-dipole-moment, under different temperatures and for different aligning field strengths.

The core of my work was then presented: how to analyze a composite that the NRs inside it are partially aligned, according to the angular-distribution-function that was derived. I derived the equations for such a composite, both for the permittivity and for the third order NL susceptibility. After the derivations, I presented some results that examine first the influence of the capsule shape model and then the influence of different parameters on the composite macroscopic characteristics: the single NR volume and axes aspect-ratio, and the temperature in which the NRs are aligned.

The last part of my work was to use the results obtained, to characterize a NL waveguide, with a core made of the NRs composite. I presented two basic concepts regarding NL waveguides – the effective modal area and the NL parameter of the waveguide. I examined the dependency of the effective modal area on the waveguide core dimensions, where smaller effective modal area means larger NL parameter for the NL waveguide. I examined different sizes of WG cores, to optimize the NL parameter of the waveguide. In the end I showed the influence of the aligning field strength used, on the refractive indices and NL parameters of the waveguide in the two polarizations of the optical electric field. I showed also the statistical characteristics of the waveguide, by presenting the standard-deviation of the results.

Conclusions

I will divide the conclusions of my work, into three topics: composite characteristics for a nematic array, influence of the alignment mechanism on the composite characteristics and NL waveguide (WG) characteristics.

(a) Nematic array composite:

Before looking at the macroscopic characteristics of a composite with a nematic array of NRs inside it, I wish to summarize the conditions for the single NR that my model deals with. The minimum dimension of the NR, meaning its short-axis (SA), must be above twice the Bohr radius of the bulk exciton of the material in question, to avoid quantum confinement effects. For CdSe NRs, the Bohr radius of the bulk exciton is 5.7nm, meaning the NR SA must be above 11.4nm. I considered NRs with a SA longer than 12nm. On the other hand, the long-axis (LA) of the NR must fulfill the condition for homogenization of the composite: $LA < \lambda / \left(2\pi \cdot n_{eff}\right)$, where λ / n_{eff} is the optical electric field wavelength in the composite. For my case $\lambda = 1550nm$ resulting with $LA < 160nm$.

Regarding the nematic array composite, for a given volume fill fraction, the important parameter of the NRs is their axes aspect ratio (AR), when high AR reduces the NRs depolarization factor. For high values of third order susceptibility of the composite, NRs with high AR (low depolarization factor) are needed, meaning elongated NRs. Increasing the AR of the single NR, from 6 to 30, increases the value of the susceptibility (in percentage from the NRs susceptibility) for a nematic array composite, from 2.73% to 3.75%. The single NR volume does not affect the composite, since the volume fraction of the NRs in the composite is set as constant (I used 4%). The model for describing the NRs as capsule shapes, increased the NRs depolarization factor, thus reducing the composite NL susceptibility, for a nematic array.

(b) The alignment mechanism

The alignment mechanism depends strongly on the single NR volume and hardly on the single NR axes AR. The model of the capsule shape results with stronger alignment, due to the larger volume of a capsule shape compared to a prolate spheroid, for a given length and width. The temperature of the polymerization can influence the alignment too, where higher temperatures cause larger thermal fluctuations which makes the alignment harder. Looking at the results for the third order susceptibility, I defined a measure for the alignment strength: the aligning field strength required to bring the susceptibility half the way from the value of random orientation to the value of nematic array.

For the influence of the single NR volume, I showed how the required field strength falls like the inverse of the volume. For NRs AR of 10, enlarging the single NR volume from 13,100nm^3 (120×12nm, length×width) to 44,200^3 (180×18, length×width. 3.75 times larger) resulted with required field strength about 3 times smaller (from 10^6 V/m to 3×10^5V/m).

For the influence of the polymerization temperature, I showed that reducing the temperature from 200°C to 125°C, reduces the aligning field strength required, from 1.8×10^6 V/m to 9.7×10^5V/m (46% less).

The single NR axes AR effect on the alignment, is negligible. However, for no alignment, meaning a random orientation composite, I showed that the AR of the single NR is a meaningful parameter. Increasing the AR from 6 to 30, increases the value of the susceptibility (in percentage from the NRs susceptibility) for random orientation composite, from 1.18% to 1.51%. Spherical inclusions will have a third order susceptibility of only 0.61%.

(c) NL waveguide characteristics

The main characteristic of a NL WG is the NL parameter. This parameter depends on the NL material – its third order susceptibility, and on the WG effective modal area. The third order susceptibility was addressed in the two former sections of the conclusions. The effective modal area depends mainly on the WG core dimensions. I examined a composite with NRs dimensions of 120×12nm, (length×width) and again volume fraction of 4%. The required field for this composite (as described above) is $\bar{E} = 10^6 V/m$. I showed that the optimized shape for the NL WG is a square core, and show that the dimensions of 1.3×1.3µm^2 for the core are ideal, resulting with effective modal area of 2.6 µm^2. Changing the dimensions to 1.5×1.5µm^2 (which was successfully fabricated in the past), increases the effective modal area to 2.7µm^2 – a change of 3.8%. The resulting NL parameter for the NL WG is $\gamma = 119(W\cdot m)^{-1}$ for 1.5×1.5µm^2 core WG and $\gamma = 120.5(W\cdot m)^{-1}$ for 1.3×1.3µm^2 core WG – 1.2% enhancement. The difference between the two dimensions is small, meaning there is no necessity to pursue 1.3×1.3µm^2 core WG, although it is better. These values for the NL parameter are very high, comparing to glass based NL optical fibers. The resulted NL parameter for random orientation composite is $\gamma = 68.6\left(W \cdot m\right)^{-1}$ which is also a good result comparing to common NL WGs.

I showed also the birefringence of the WG, varying between zero (for random orientation) and 0.022 (nematic array). The birefringence for the required field strength is $\Delta n = 0.0108$. The last thing I showed was the statistical behavior of the result, in both polarization directions. I showed the standard deviation of the values of the NL parameters and in order to avoide the possibility of same results for both polarization directions, the aligning field strength must be above 9.6×10^{5} V/m. For an aligning field of just 10^{6}V/m the result for polarization along the LA direction was very high: $\gamma = 119\left(W \cdot m\right)^{-1}$, and for the SA direction $\gamma = 42\left(W \cdot m\right)^{-1}$.

It is important to note, that changing the volume of the single NR or its axes AR will result with even higher values for the NL parameter. However the limitation on the maximum NR length has to be fulfilled, otherwise diffraction and scattering of the optical signal will become significant.

Appendix A: Derivation of the polarizability

I will start the derivation of the polarizability, with the simplest case of an isotropic inclusion of a sphere in which, ignoring crystallographic anisotropy, α is a scalar. The surrounding and inclusion permittivities are $\varepsilon_h, \varepsilon_i$ respectively, and the internal field inside the sphere is assumed to be uniform and it is given by [7]:[5]

$$E_{in} = \frac{3\varepsilon_h}{\varepsilon_i + 2\varepsilon_h} E_{ext} \tag{A.1}$$

For a more complicated shape as an ellipsoid, the internal field depends on the direction of the external field regarding the ellipsoid major axes. For a field along such an axis, the internal field is given by:

$$E_{in} = \frac{\varepsilon_h}{\varepsilon_h + L^j\left(\varepsilon_i - \varepsilon_h\right)} E_{ext} \tag{A.2}$$

where L^j is the "depolarization factor" of the ellipsoid in the $j = x, y, z$ directions, which are the major axes of the ellipsoid. The depolarization factor is derived from solving the electric potential of the ellipsoid and is defined as [15]:

$$L^j = \frac{a_x a_y a_z}{2} \int_0^\infty \frac{ds}{\left(s + a_j^2\right)\sqrt{\left(s + a_x^2\right)\left(s + a_y^2\right)\left(s + a_z^2\right)}} \tag{A.3}$$

where s is a length element in the direction in interest and a_x, a_y, a_z are the three semi-axes of the ellipsoid. The three depolarization factors in the three directions satisfy $L^x + L^y + L^z = 1$. For a sphere the depolarization factors are $L^x = L^y = L^z = 1/3$, hence Eq. (A.1) can be derived from Eq. (A.2). For the case of ellipsoid of revolution (ellipsoid with two equal semi-axes, which is called a spheroid), there is a closed form for the depolarization factors. I will present only the result for a prolate spheroid (two equal SAs and one LA). I chose the $\hat{z}$ axis as the LA of the spheroid and therefore $\hat{x}, \hat{y}$ are the SAs of the spheroid. The depolarization factors for a prolate spheroid are:

---

[5] Sihvola assumes this field and then show that it is satisfying the curl free condition for the electric field and boundary condition with the field in the sphere surrounding. See also Appendix B.

$$L^z = L^{LA} = \frac{1-e^2}{e^2}\left(\frac{1}{2e}\ln\left(\frac{1+e}{1-e}\right)-1\right) \quad , \quad L^x = L^y = L^{SA} = \frac{1-L^{LA}}{2} \tag{A.4}$$

where $e = \sqrt{1-a_x^2/a_z^2}$ is the eccentricity of the prolate spheroid and according to my notation $a_z > a_x = a_y$ [7,15].

As explained, the polarization density inside the inclusion, can be derived from the internal field. There are two approaches to define the polarization density $\vec{P}$ from the internal field. The first approach presented by Landau and Lifshitz, presented in Gaussian unit system, is [15]:

$$\vec{P} = \frac{1}{4\pi}\frac{(\varepsilon_i - \varepsilon_h)}{\varepsilon_h}\vec{E}_{in} \tag{A.5}$$

According to my notation for the vacuum permittivity, in SI unit system, the polarization density will be:

$$\vec{P} = \varepsilon_0 \frac{(\varepsilon_i - \varepsilon_h)}{\varepsilon_h}\vec{E}_{in} \tag{A.5.a}$$

Stratton [42], followed by Sihvola [7] on the other hand, derived the polarization density at SI unit system and defined the polarization density without the normalization by ε_h:

$$\vec{P} = \varepsilon_0 (\varepsilon_i - \varepsilon_h)\vec{E}_{in} \tag{A.6}$$

Later on I will address the question of which formula suits my work better. According to both approaches, after finding the polarization density, the polarizability can be derived. All of the mentioned authors assume homogeneous polarization density inside the inclusion, and the dipole moment is defined as $\vec{\mu} = V \cdot \vec{P}$. As explained, α is a second rank tensor and again ignoring crystallographic anisotropy, assumed to have only three diagonal elements. The polarizability for an ellipsoid according to Landau and Lifshitz is:

$$\alpha_{Landau\&Lifshitz} = V\varepsilon_0 \frac{(\varepsilon_i - \varepsilon_h)}{\varepsilon_h + L^j(\varepsilon_i - \varepsilon_h)} \tag{A.7}$$

and according to Sihvola:

$$\alpha_{Sihvola} = V\varepsilon_0 \frac{(\varepsilon_i - \varepsilon_h)}{\varepsilon_h + L^j (\varepsilon_i - \varepsilon_h)} \varepsilon_h \tag{A.8}$$

Ruda and Shik used Landau and Lifshitzs' formula (Eq. (A.7)), in Gaussian unit system, with a reduction of the $1/4\pi$ factor [12]. Li and Alivisatos converted this equation into SI unit system simply by replacing the factor of $1/4\pi$ with ε_0 [25].

The two equations converge in two points: (a) In the case the inclusion is in vacuum, $\varepsilon_h = 1$: $\vec{P}_{in} = \varepsilon_0 (\varepsilon_i - 1) \vec{E}_{in}$. (b) In the case the permittivity of the inclusion equals the permittivity of the host, $\varepsilon_h = \varepsilon_i$: $\vec{P}_{in} = 0$. From the second case it is understood that the polarization density in question is the polarization density above that of the background (host), hence even in the case that $\varepsilon_h = \varepsilon_i > 1$, the polarization density inside is considered to be zero. I simulated a prolate spheroid under a uniform external field and extracted the polarization density inside the spheroid. I subtracted the polarization density of the background (far from the spheroid) from the result of the polarization density inside the spheroid. The simulations were performed in 3D, but the results are presented in 2D slices, in the y-z plane (Fig, A.1.a). The uniform external field was applied with a large capacitor, as shown in Fig. A.1.a as an example.

The parameters used in the simulations – permittivities: $\varepsilon_h = 5$, $\varepsilon_i = 10$, spheroid semi-axes: $a = 30nm$, $b = 6nm$, external field: 10V/m. In Fig. A.1.b, I present a zoom in on the spheroid and in Fig. A.1.c the results along the $\hat{z}$ axis.

(a) Polarization density y-z plane

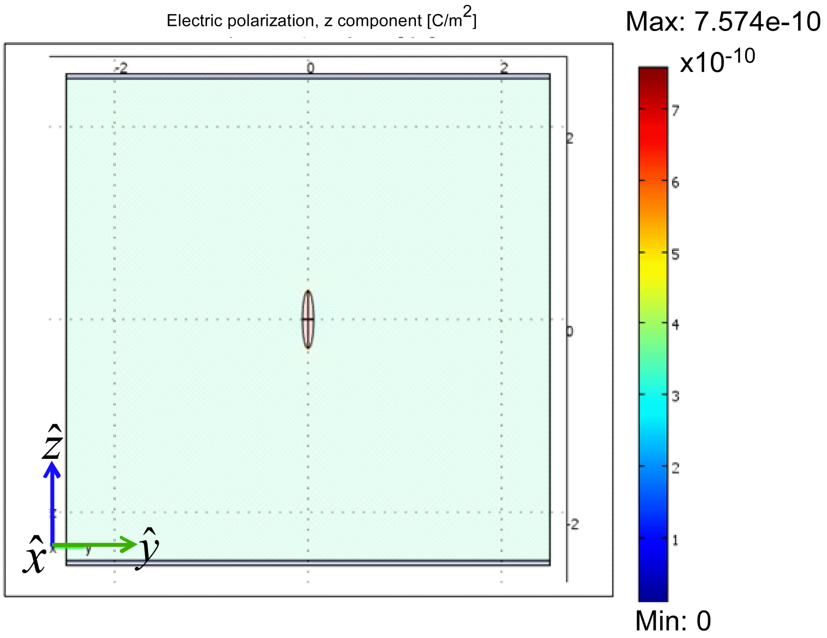

(b) Polarization density y-z plane zoom in

(c) Polarization density along the z axis

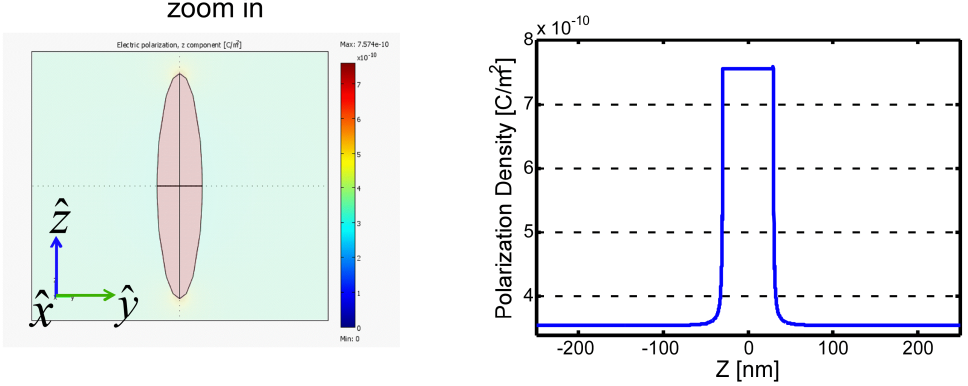

Fig A.1. Simulation result from COMSOL for the polarization density of a prolate spheroid inside a large capacitor. Parameters used: $a = 30nm$, $b = 6nm$, $\varepsilon_h = 5$, $\varepsilon_i = 10$, $E_{ext} = 10V/m$: (a) Presentation of the $\hat{y} - \hat{z}$ plane. (b) Zoom in on the spheroid. (c) Results along the $\hat{z}$ axis.

I simulated the same spheroid with the same permittivity and changed the host permittivity from vacuum ($\varepsilon_h = 1$) to the inclusion permittivity ($\varepsilon_h = 10$). I compared the results of the polarization density (minus the background polarization density) from the simulations to the results of the formulas of Sihvola and of Landau and Lifshitz. The comparison is presented in Fig. A.2.

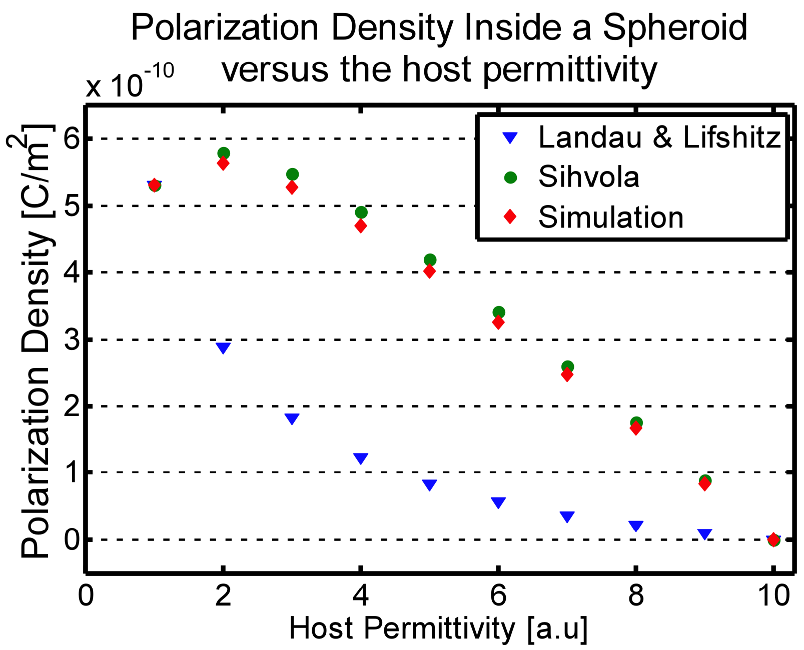

Fig A.2 Comparison of the results for the polarization density inside the spheroid, between Landau and Lifshitz, Sihvola and the simulations. Parameters chosen: $a = 30nm$, $b = 6nm$, $\varepsilon_i = 10$, $E_{ext} = 10V/m$.

The results clearly show that the formula given by Sihvola suits the simulations much better than that of Landau and Lifshitz. The average deviation of the results of Sihvola from those of the simulations (ignoring the two end points $\varepsilon_h = 1$ and $\varepsilon_h = \varepsilon_i = 10$) is 4.5%. For Landau and Lishitz the average deviation is 76%. Given these results I chose to use the formula for the polarizability given by Sihvola (Eq. (A.8) which is also Eq. (2.2) in section 2.1.1).

Appendix B: Hyperpolarizability of a sphere and an ellipsoids

In this appendix, I present the derivation made by Sihvola for calculating the first and second order hyperpolarizability of a sphere [7] and following his leads, the same derivation for an ellipsoid.

I will start from Sihvola's analysis for the internal field $\vec{E}_i$ inside an inclusion under an external electric field $\vec{E}_{ext}$. The internal field is a sum of the external field and the "scattered" field $\vec{E}_s$, cause by the induced polarization density field $\vec{P}$:

$$\vec{E}_i = \vec{E}_{ext} + \vec{E}_s \tag{B.1}$$

Sihvola finds the relation between the scattered field and the polarization density to be:

$$\vec{E}_s = -\frac{1}{\varepsilon_h}\vec{\vec{L}}\cdot\vec{P} \tag{B.2}$$

where ε_h is the permittivity of the environment and $\vec{\vec{L}}$ is the depolarization factor, which like the polarizability is a second order tensor. The internal field is therefore:

$$\vec{E}_i = \vec{E}_{ext} - \frac{1}{\varepsilon_h}\vec{\vec{L}}\cdot\vec{P} \tag{B.3}$$

For a sphere inclusion the depolarization is a scalar – $L = 1/3$.

Hyperpolarizability of a sphere:

For a NL material, the polarization $\vec{P}$ is usually presented as a power series in the electric field $\vec{E}$:

$$\vec{P} = \varepsilon_0\left(\chi^{(1)}\vec{E} + \chi^{(2)}\vec{E}^2 + \chi^{(3)}\vec{E}^3 + \ldots\right) \tag{B.4}$$

In this presentation, the tensorial characteristics of the susceptibilities are not presented explicitly, but it can be addressed by treating each susceptibility as a tensor, and using a tensor multiplication. Assuming the linear susceptibility is a scalar, the internal polarization density in a sphere can be presented as:

$$\vec{P}_i = \varepsilon_0 \left(\varepsilon_i - \varepsilon_h \right) \vec{E}_i + \varepsilon_0 \left(\chi^{(2)} \vec{E}_i^2 + \chi^{(3)} \vec{E}_i^3 + \ldots \right) \tag{B.5}$$

where again the permittivities of the sphere inclusion and environment are $\varepsilon_i, \varepsilon_h$ respectively. The dipole moment of the sphere is also NL and is a function of the external field:

$$\vec{\mu} = \alpha \vec{E}_{ext} + \beta \vec{E}_{ext}^2 + \gamma \vec{E}_{ext}^3 + \ldots \tag{B.6}$$

According to Eq. (B.3), for a sphere inclusion the internal field will be $\vec{E}_i = \vec{E}_{ext} - \vec{P}/3\varepsilon_e$ or $\vec{P} = 3\varepsilon_e \left(\vec{E}_{ext} - \vec{E}_i \right)$. Using this expression for the polarization density inside Eq. (B.5) and isolating the linear term of the internal field, will result with:

$$\vec{E}_i = \frac{3\varepsilon_h}{\varepsilon_i + 2\varepsilon_h} \vec{E}_{ext} - \frac{\varepsilon_0}{\varepsilon_i + 2\varepsilon_h} \left(\chi^{(2)} \vec{E}_i^2 + \chi^{(3)} \vec{E}_i^3 + \ldots \right) \tag{B.7}$$

At this point, Sihvola assumes the "linear approximation", and uses the linear term for the internal field (as a function of the external field) in the powers inside Eq. (B.7).The linear field is:

$$\vec{E}_i = \frac{3\varepsilon_h}{\varepsilon_i + 2\varepsilon_h} \vec{E}_{ext} \tag{B.8}$$

hence Eq. (B.7) is approximated to:

$$\vec{E}_i \approx \frac{3\varepsilon_h}{\varepsilon_i + 2\varepsilon_h} \vec{E}_{ext} - \frac{\varepsilon_0}{\varepsilon_i + 2\varepsilon_h} \left[\left(\frac{3\varepsilon_h}{\varepsilon_i + 2\varepsilon_h} \right)^2 \chi^{(2)} \vec{E}_{ext}^2 + \left(\frac{3\varepsilon_h}{\varepsilon_i + 2\varepsilon_h} \right)^3 \chi^{(3)} \vec{E}_{ext}^3 + \ldots \right] \tag{B.9}$$

He uses Eq. (B.9) for the internal field inside the expression $\vec{P} = 3\varepsilon_e \left(\vec{E}_{ext} - \vec{E}_i \right)$ from Eq. (B.3) for a sphere and remembering that $\vec{\mu} = V \cdot \vec{P}$ the result is:

$$\begin{aligned}\vec{\mu} &= V\frac{\left(\varepsilon_i-\varepsilon_h\right)}{\varepsilon_i+2\varepsilon_h}3\varepsilon_0\varepsilon_h\vec{E}_{ext}+\\ &+V\left(\frac{3\varepsilon_h}{\varepsilon_i+2\varepsilon_h}\right)^3\varepsilon_0\chi^{(2)}\vec{E}_{ext}^2+V\left(\frac{3\varepsilon_h}{\varepsilon_i+2\varepsilon_h}\right)^4\varepsilon_0\chi^{(3)}\vec{E}_{ext}^3+\ldots\end{aligned} \tag{B.10}$$

From this equation, the polarizability and hyperpolarizabilties can be identified easily.

Hyperpolarizability of an ellipsoid:

The derivation for ellipsoids requires Eq. (B.3) without reducing the depolarization factor by $L=1/3$. The expression $\vec{P}=3\varepsilon_h\left(\vec{E}_{ext}-\vec{E}_i\right)$ becomes $P^j=\frac{\varepsilon_h}{L^j}\left(E_{ext}-E_i^j\right)$ which is direction dependant, according to the external field direction ($j=x,y,z$). Eq. (B.7) becomes:

$$E_i^j=\frac{\varepsilon_h}{\left(\varepsilon_i-\varepsilon_h\right)L^j+\varepsilon_h}E_{ext}-\frac{L^j}{\left(\varepsilon_i-\varepsilon_h\right)L^j+\varepsilon_h}\left(\chi^{(2)}\left(E_i^j\right)^2+\chi^{(3)}\left(E_i^j\right)^3+\ldots\right) \tag{B.11}$$

and Eq. (B.8) becomes:

$$E_i^j=\frac{\varepsilon_h}{\left(\varepsilon_i-\varepsilon_h\right)L^j+\varepsilon_h}E_{ext} \tag{B.12}$$

Following the same derivation as for the case of a sphere, Eq. (B.10) becomes:

$$\begin{aligned}\mu^j &= V\frac{\left(\varepsilon_i-\varepsilon_h\right)}{\varepsilon_h+L^j\left(\varepsilon_i-\varepsilon_h\right)}\varepsilon_0\varepsilon_h E_{ext}+\\ &+V\left(\frac{\varepsilon_h}{\varepsilon_h+L^j\left(\varepsilon_i-\varepsilon_h\right)}\right)^3\varepsilon_0\chi^{(2)}E_{ext}^2+V\left(\frac{\varepsilon_h}{\varepsilon_h+L^j\left(\varepsilon_i-\varepsilon_h\right)}\right)^4\varepsilon_0\chi^{(3)}E_{ext}^3\end{aligned} \tag{B.13}$$

Again, from the last equation, the polarizability and hyperpolarizabilities can be identified easily.

Appendix C: derivation of the MG model by Sihvola

There are several ways to derive the MG model for composite with linear sphere inclusions [6,7,17,19]. I will present the derivation given by Sihvola which uses average values of the macroscopic fields in the composite [7].

Sihvola starts from the macroscopic displacement field (electric flux density in his notation):

$$\left\langle \vec{D} \right\rangle = \varepsilon_{eff} \left\langle \vec{E} \right\rangle = \varepsilon_h \left\langle \vec{E} \right\rangle + \left\langle \vec{P} \right\rangle \tag{C.1}$$

The average polarization density evolves from the dipole moments in the mixture $\vec{\mu}_{mix}$:

$$\left\langle \vec{P} \right\rangle = n \cdot \vec{\mu}_{mix} \tag{C.2}$$

where n is the number density of the dipoles. It is important to notice that the dipole moment in the mixture is different from a single induced dipole moment, because of the influence of all the other dipoles on the average electric field. The local field near the inclusion is given by the external field and the average polarization density in the mixture:

$$\vec{E}_L = \left\langle \vec{E} \right\rangle + \frac{1}{3\varepsilon_h} \left\langle \vec{P} \right\rangle \tag{C.3}$$

where the factor $1/3$ is the depolarization factor of a sphere. The single induced dipole moment in the mixture is then:

$$\vec{\mu}_{mix} = \alpha \vec{E}_L \tag{C.4}$$

where α is the single inclusion polarizability. Combining Eqs. (C.2) and (C.4) results with:

$$\left\langle \vec{P} \right\rangle = n \cdot \alpha \cdot \vec{E}_L \tag{C.5}$$

Then, using Eq. (C.3) for the local field, inside Eq. (C.5) the polarization density can be extracted:

$$\left\langle \vec{P} \right\rangle = \frac{n \cdot \alpha}{1 - \dfrac{n \cdot \alpha}{3 \cdot \varepsilon_h}} \cdot \left\langle \vec{E} \right\rangle \tag{C.6}$$

Using this expression inside Eq. (C.1), we can eliminate the expressions of the average field and extract the effective permittivity:

$$\varepsilon_{eff} = \varepsilon_h + \frac{n \cdot \alpha}{1 - \dfrac{n \cdot \alpha}{3 \cdot \varepsilon_h}} \tag{C.7}$$

There are several methods to present the last equation for the effective permittivity. In the form of the polarizability, it can be presented as:

$$\frac{\varepsilon_{eff} - \varepsilon_h}{\varepsilon_{eff} + 2 \cdot \varepsilon_h} = \frac{n \cdot \alpha}{3 \cdot \varepsilon_h} \tag{C.8}$$

which is the Clausius-Mossoti formula. On the other hand, from Eq. (2.2) (or A.8) for the polarizability of an ellipsoid the polarizability of a sphere can be found (by using $L = 1/3$):

$$\alpha_{sphere} = V\left(\varepsilon_i - \varepsilon_h\right) \frac{3 \cdot \varepsilon_h}{\varepsilon_i + 2 \cdot \varepsilon_h} \tag{C.9}$$

Then by using the expression for the polarizability inside Eq. (C.8) the effective permittivity can be presented in terms of the permittivities and volume fraction, by remembering that $p = n \cdot V$. The effective permittivity is given by simple algebra:

$$\varepsilon_{eff} = \varepsilon_h + 3 \cdot p \cdot \varepsilon_h \frac{\varepsilon_i - \varepsilon_h}{\varepsilon_i + 2 \cdot \varepsilon_h - \left(\varepsilon_i - \varepsilon_h\right) p \cdot} \tag{C.10}$$

which is the same as Eq. (2.9) – Maxwell-Garnett formula.

Appendix D: different approaches and assumptions for the NL Maxwell-Garnett model

As explained in section 2.2.2, several approaches were presented for the derivation of the generalization of the MG model for NL inclusions. I will present the method, assumption and conclusion of three authors, without presentation of the whole derivation. More approaches can be found in the review of Gehr and Boyd [18].

Ricard *et al*. were the first to derive a generalization for the MG model, dealing with the nonlinearity of metal spheres dispersed in water [43]. They used a presentation of the linear MG model as:

$$\frac{\varepsilon_{eff}-\varepsilon_h}{\varepsilon_{eff}+2\cdot\varepsilon_h}=p\cdot\beta\ ,\ \beta=\frac{\varepsilon_i-\varepsilon_h}{\varepsilon_i+2\cdot\varepsilon_h} \tag{D.1}$$

and taking the result for the effective permittivity to the lowest order in the volume fraction p, they obtain:

$$\varepsilon_{eff}=\varepsilon_h\left(1+3p\cdot\beta\right) \tag{D.2}$$

Expanding the result to Taylor series for a small deviation in the inclusions permittivity, results with:

$$\delta\varepsilon_{eff}=3\varepsilon_h p\frac{\partial\beta}{\partial\varepsilon_i}\delta\varepsilon_i \tag{D.3}$$

Assuming the change in the inclusions permittivity is due to the third order nonlinearity and using the internal field inside the sphere inclusion (Eq. (A.1)) as the local field experienced by the inclusion, they found:

$$\chi_{eff}^{(3)}=\delta\varepsilon_{eff}=p\left(\frac{3\varepsilon_h}{\varepsilon_i+2\varepsilon_h}\right)^2\left|\frac{3\varepsilon_h}{\varepsilon_i+2\varepsilon_h}\right|^2\chi_i^{(3)} \tag{D.4}$$

Sipe and Boyd presented a method to derive the MG model (linear and sphere inclusions) by addressing the mesoscopic fields in the composite, meaning the field that a single inclusion "feels" [19]. After calculating the MG model, they expanded their derivations for the cases of NL inclusion and/or NL host. Like Ricard *et al*. their work is also entirely for sphere inclusions and I will only present the final result for the NL inclusion case. They use the notation of the electric displacement field (in Gaussian unit system):

$$\vec{D}(\vec{r}) = \varepsilon\vec{E}(\vec{r}) + 4\pi A\left[\vec{E}(\vec{r})\cdot\vec{E}(\vec{r})^{*}\right]\vec{E}(\vec{r}) + 2\pi B\left[\vec{E}(\vec{r})\cdot\vec{E}(\vec{r})\right]\vec{E}(\vec{r})^{*} \tag{D.5}$$

where the coefficients A and B are related to the third order NL susceptibility tensor components: $A = 6\chi_{1122}$ and $B = 6\chi_{1221}$ (see [16]). The relation between the composite effective coefficients (A, B) and the inclusions coefficients (A^i, B^i), is given by [19]:

$$A = f\left|\frac{\varepsilon_{eff} + 2\varepsilon_h}{\varepsilon_i + 2\varepsilon_h}\right|^2\left(\frac{\varepsilon_{eff} + 2\varepsilon_h}{\varepsilon_i + 2\varepsilon_h}\right)^2 A^i \ , B = f\left|\frac{\varepsilon_{eff} + 2\varepsilon_h}{\varepsilon_i + 2\varepsilon_h}\right|^2\left(\frac{\varepsilon_{eff} + 2\varepsilon_h}{\varepsilon_i + 2\varepsilon_h}\right)^2 B^i \tag{D.6}$$

where ε_{eff} is the effective permittivity, given by the linear MG model. The main difference between the result of Sipe and Boyd to that of Ricard *et al.* is the expression in the numerators of $\left(\varepsilon_{eff} + 2\varepsilon_h\right)$ instead of $\left(3\varepsilon_h\right)$.

Lamarre *et al.* followed the method presented by Ricard *et al*. and derived first an expression for ellipsoid inclusions [6]. They used the linear generalization of the MG model for ellipsoid inclusions (Eq. (2.10)) that for the first order approximation in the volume fraction (assuming $p << 1$) is:

$$\varepsilon_{eff}^{j} \cong \varepsilon_h + p\frac{\varepsilon_h\left(\varepsilon_i - \varepsilon_h\right)}{L^j\varepsilon_i + \left(1 - L^j\right)\varepsilon_h} \tag{D.7}$$

Following the method presented by Ricard *et al*. with the same assumptions, they found:

$$\chi_{eff}^{(3),j} = p\left(\frac{\varepsilon_h}{L^j\varepsilon_i + \left(1 - L^j\right)\varepsilon_h}\right)^2\left|\frac{3\varepsilon_h}{L^j\varepsilon_i + \left(1 - L^j\right)\varepsilon_h}\right|^2 \chi_i^{(3)} \tag{D.8}$$

Using the same derivation for larger volume fraction they used the full expression of Eq. (2.10) for the effective permittivity of a composite with ellipsoid inclusions. Their result is:

$$\chi_{eff}^{(3),j} = p\left(\frac{\varepsilon_h}{L^j\varepsilon_i + \left(1-L^j\right)\varepsilon_h - p\left(\varepsilon_i - \varepsilon_h\right)}\right)^2 \left|\frac{3\varepsilon_h}{L^j\varepsilon_i + \left(1-L^j\right)\varepsilon_h}\right|^2 \chi_i^{(3)} \tag{D.9}$$

The difference between the large and small volume fraction (Eqs. (D.8) and (D.9)), is in the additional expression of $\left[-p\left(\varepsilon_i - \varepsilon_h\right)\right]$ in the denominator of the first expression on the right hand side of Eq. (D.9).

Sihvoal used the average quantities of the different macroscopic fields:

$$\left\langle \vec{D} \right\rangle = \varepsilon_h \left\langle \vec{E} \right\rangle + \left\langle \vec{P} \right\rangle = \varepsilon_{eff} \left\langle \vec{E} \right\rangle + \varepsilon_0 \left[\chi_{eff}^{(2)} \left\langle \vec{E} \right\rangle \left\langle \vec{E} \right\rangle + \chi_{eff}^{(3)} \left\langle \vec{E} \right\rangle \left\langle \vec{E} \right\rangle \left\langle \vec{E} \right\rangle + \ldots\right] \tag{D.10}$$

where the epxression ε_{eff} here, stands for the linear effective permittivty only. For sphere inclusions and small volume fraction, Sihvola assumes that the field that excite an inclusion is the average field $\left\langle \vec{E} \right\rangle$, hence the effective parameters depends on the polarizability α and hyperpolarizabilities β, γ. The effective susceptibilities are:

$$\begin{aligned} \chi_{eff}^{(2)} &= n\beta/\varepsilon_0 \\ \chi_{eff}^{(3)} &= n\gamma/\varepsilon_0 \end{aligned} \tag{D.11}$$

For the third order nonlinearity, using the expression for γ from Eq. (B.10), the result for a sphere inclusions is:

$$\chi_{eff}^{(3)} = p\left(\frac{3\varepsilon_h}{\varepsilon_i + 2\varepsilon_h}\right)^4 \chi_i^{(3)} \tag{D.12}$$

Deriving the same for ellipsoid inclusions, with the hyperpolarizability of an ellipsoid as derived in Appendix B, results with:

$$\chi_{eff}^{(3),j} = p\left(\frac{\varepsilon_h}{L^j\varepsilon_i + \left(1-L^j\right)\varepsilon_h}\right)^4 \chi_i^{(3)} \tag{D.13}$$

It is important to mention that Sihvola derived all of his derivations for dielectric inclusions. The models presented by by Ricard *et al.* Lamarre *et al.* and Sipe and Boyd were derived for metal inclusions. Nevertheless, they can be used with dielectric inclusions [18], hence the result I presented following Sihvola, is the same as the result presentes by Lamarre *et al.* for small volume fraction (Eq. (D.8)), for dielectric material (i.e with a real value for the permittivities).

It is interesting to examine the difference between the models for the large and small volume fractions (Eqs. (D.8.) and (D.13) compared to Eq. (D.9)). I will use parameters values of $\varepsilon_i = 6.2$, $\varepsilon_h = 2.19$ as before and $L^{LA} = 0.1$, $L^{SA} = 0.45$, and examine the influence of the volume fraction p on the value of $\chi_{eff}^{(3),j} \big/ \chi_i^{(3)}$ for the two forms. In Fig. D.1.a, I present the values of the two equations as a function of the volume fraction, between the values of 0 and 20% for the volume fraction (which is the MG model limit). In Fig. D.1.b, I present the deviation of the small volume fraction equation, relative to the equation for large volume fraction, in percentage. It can be seen from Fig D.1.b, that the deviation of the values from the small volume fraction equation, grows almost linearly with the volume fraction itself. For the value $p = 4\%$ that I used in my work, the deviation is 1.23%, which justifies in my opinion the use of the small volume fraction equation – Eq. (D.13) throughout my work.

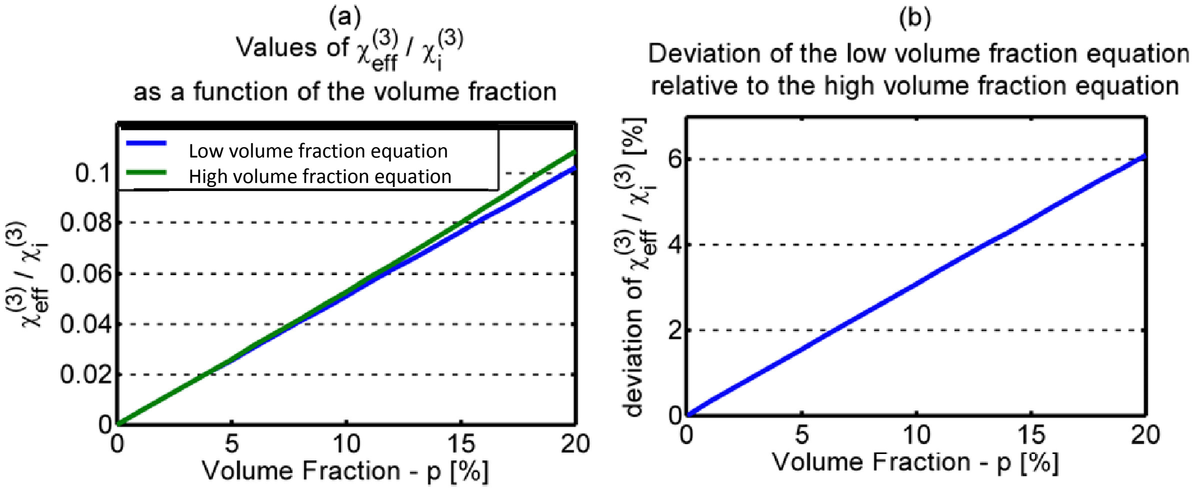

Fig. D.1: Comparison between the values of the effective third order NL susceptibility of a composite with ellipsoid inclusions as a function of the volume fraction. (a) Values of the composite effective susceptibility normalized by the inclusions susceptibility, for the two equations. (b) The deviation of the values of the equation for low volume fraction, relative to the values of the equation for high volume fraction.

References

[1] F. Trani, "Polarization anisotropy in the optical properties of silicon ellipsoids", Surf. Sci. **601**, 2702-2706 (2007)

[2] J. Valenta, B. Bruhn and Jan Linnros, "Polarization of photoluminescence excitation and emission spectra of silicon nanorods within single Si/SiO2 nanowires", Phys. Status Solidi C **8**, 1017-1020 (2011)

[3] Y. K. Olsson, G. Chen, R. Rapaport, D. T. Fuchs, V. C. Sundara, J. S. Steckel, M. G. Bawendi, A. Aharoni and U. Banin, "Fabrication and optical properties of polymeric waveguides containing nanocrystalline quantum dots", Appl. Phys. Lett. **85**, 4469-4471 (2004)

[4] G. Chen,R. Rapaport, D. T. Fuchs, L. Lucas, A. J. Lovinger, S. Vilan, A. Aharoni and U. Banin, "Optical gain from InAs nanocrystal quantum dots in a polymer matrix", Appl. Phys. Lett. **87**, 251108-251110 (2005)

[5] C. Sciancalepore, T. Cassano, M. L. Curri, D. Mecerreyes, A. Valentini, A. Agostiano, R. Tommasi and M. Striccoli, "TiO2 nanorods/PMMA copolymer-based nanocomposites: highly homogeneous linear and nonlinear optical material", Nanotechnology **19**, 205705 (2008)

[6] J. M. Lamarre, F. Billard and L. Martinu, "Local field calculations of the anisotropic nonlinear absorption coefficient of aligned gold nanorods embedded in silica", J. Opt. Soc. Am. B **25**, 961-971 (2008)

[7] A. H. Sihvola, *Electromagnetic Mixing Formulas and Applications*, (The Institution of Engineering and Technology, London, 2008)

[8] S. Giordano, "Effective medium theory for dispersions of dielectric ellipsoids", J. Electrostat. **58**, 59–76, (2003)

[9] B. Weintraub, Y. Deng and Z. L. Wang, "Position-Controlled Seedless Growth of ZnO Nanorod Arrays on a Polymer Substrate via Wet Chemical Synthesis", J. Phys. Chem. C, **111**, 10162-10165 (2007)

[10] C. C. Lai, Y. J. Lee, P. H. Yeh and S. W. Lee "Formation mechanism of SiGe nanorod arrays by combining nanosphere lithography and Au-assisted chemical etching", Nanoscale Research Letters, **7**, (2012)

[11] A. H. Sihvola and J. A. Kong, "Effective permittivity of dielectric mixtures", IEEE T. Geosci. Remote. **26**, 420-429 (1988)

[12] H. E. Ruda and A Shik, "Nanorod dynamics in ac electric fields", Nanotechnology **21** 235502 (2010)

[13] A. Adler and D. M. Marom, “High Index Contrast Polymer Optical Waveguides”, IEEE Israel 2010, Eilat, Israel, Nov. 2010.

[14] A. Adler and D. M. Marom, “High Index Contrast Polymer Optical Waveguides”, Conference on Lasers and Electro-optics (CLEO ‘11), Baltimore, MD, May 2011.

[15] L.D. Landau and E.M Lifshitz, *Electrodynamics of Continuous Media*, 2nd ed.(Pergamon Press, Oxford, 1984), Chap. 8

[16] R. W. Boyd, *Nonlinear Optics*, 2nd ed.(Academic Press, San Diego, 2003)

[17] J. C. Maxwell-Garnett, "Colours in Metal Glasses and in Metallic Films", Philos. Trans. R. Soc. London, Ser. A **203**, 385-420 (1904).

[18] R. J. Gehr and R. W. Boyd, "Optical Properties of Nanostructured Optical Materials", Chemistry of Materials, 1996, **8**, pp. 1808-1809

[19] J. E. Sipe and R.W. Boyd, "Nonlinear susceptibility of composite optical materials in the Maxwell Garnett model", Phys. Rev. A **46**, 1614-1629 (1992)

[20] R. M. Osgood Jr., N. C. Panoiu, J. I. Dadap, X. Liu, X. Chen, I-W. Hsieh, E. Dulkeith, W. M. J. Green and Y. A. Vlasov, "Engineering nonlinearities in nanoscale optical systems: physics and applications in dispersion-engineered silicon nanophotonic wires", Advances in Optics and Photonics **1**, 162–235 (2009)

[21] C. Koos, L. Jacome, C. Poulton, J. Leuthold and W. Freude, "Nonlinear silicon-on-insulator waveguides for all-optical signal processing", Opt. Express **15**, 5976–5990 (2007)

[22] C. B. Murray, C. R. Kagan and M. G. Bawendi, "Synthesis and characterization of monodisperse nanocrystals and close-packed nanocrystal assemblies", Annual Review of Materials Science, Annu. Rev. Mater. Sci. (2000) **30,** Pages: 545-610

[23] Y. Kayanuma, "Quantum-size effects of interacting electrons and holes in semiconductor microcrystals with spherical shape", Phys. Rev. B **38**, 9797-9805 (1998)

[24] M. T. Harrison, S. V. Kershaw, M. G. Burt, A. L. Rogach, A. Kornowski, A. Eychmüller, and H. Weller, "Colloidal nanocrystals for telecommunications. Complete coverage of the low-loss fiber windows by mercury telluride quantum dots", Pure Appl. Chem., Vol. 72, pp. 295–307, 2000.

[25] L. S. Li and A. P. Alivisatos, "Origin and Scaling of the Permanent Dipole Moment in CdSe Nanorods", Phys. Rev. Lett. **90**, 097402 (2003)

[26] T. Nann and J. Schneider, "Origin of permanent electric dipole moments in wurtzite nanocrystals", Chem. Phys. Lett. **384**, 150-152 (2004)

[27] H. K. Nga, Y. A. Leem, R. Knobel, I. P. Smorchkov, A. A. Sirenko and N. Samarth, "Cyclotron resonance in modulation-doped ZnSe/Zn12xCdxSe and ZnTe/CdSe single quantum wells", Appl. Phys. Lett. **75** , 3662-3664 (1999)

[28] A. Biswas and A. Ghosal, "Hole Transport Characteristics of CdSe Single Quantum Wells at Low Temperatures", Journal of Electron Devices, **10**, 444-447 (2011)

[29] C. Pecharromán, J. Pérez-Juste, G. Mata-Osoro, L. M. Liz-Marzán and P. Mulvaney, "Redshift of surface plasmon modes of small gold rods due to their atomic roughness and end-cap geometry", Phys. Rev. B **77**, 035418 (2008)

[30] C. Sönnichsen and A. P. Alivisatos, "Gold Nanorods as Novel Nonbleaching Plasmon-Based Orientation Sensors for Polarized Single-Particle Microscopy", Nano Lett. **5** 301-304 (2005)

[31] D. W. Smith, S. R. Chen, S.M. Kumar, J. Ballato, C. Topping, H. V. Shan and S. H. Foulger, "Perfluorocyclobutyl copolymers for microphotonics", Advanced Materials **14**, 1585 (2002)

[32] M. E. Schmidt, S. A. Blanton, M. A. Hines and P. Guyot-Sionnest, "Polar CdSe nanocrystals: Implications for electronic structure", J. Chem. Phys. **106**, 5254 (1997)

[33] X. L. Yang and S. W. Xie, "Expression of third-order effective nonlinear susceptibility for third-harmonic generation in crystals", Appl. Optics, **34**, 6130-6135 (1995)

[34] G. P. Agrawal, *Nonlinear Fiber Optics*, (Academic Press, San Diego, CA, 2001)

[35] Y. Zhang, W. Cheng, T. Zhang, T. Cui, Y. Wang and W. W. Yu, "Size- and Temperature-Dependent Quantum Confined Dielectric Effect in Colloidal PbSe and CdSe Nanocrystals", J. Nanosci. Nanotechno. **12**, 6224–6230 (2012)

[36] P. Petropoulos, H. Ebendorff-Heidepriem, V. Finazzi, R.C. Moore, K. Frampton, D.J. Richardson, and T.M. Monro, “Highly nonlinear and anomalously dispersive lead silicate glass holey fibers”, Opt. Express **11**, 3568-3573 (2003).

[37] H. Ebendorff-Heidepriem, P. Petropoulos, S. Asimakis, V. Finazzi, R. Moore, K. Frampton, F. Koizumi, D. Richardson, and T. Monro, “Bismuth glass holey fibers with high nonlinearity”, Opt. Express **12**, 5082-5087 (2004).

[38] V. Kumar, A. K. George, J. C. Knight, and P. S. Russell, "Tellurite photonic crystal fiber", Opt. Express **11**, 2641-2645 (2003).

[39] E. C. Mägi, L. B. Fu, H. C. Nguyen, M. R. Lamont, D. I. Yeom, and B. J. Eggleton, “Enhanced Kerr nonlinearity in sub-wavelength diameter As2Se3 chalcogenide fiber tapers”, Opt. Express **15**, 10324-10329 (2007)

[40] Y. Wang, C. Y. Lin, A. Nikolaenko, V. Raghunathan, and E. O. Potma, "Four-wave mixing microscopy of nanostructures", Advances in Optics and Photonics, **3**, 1–52 (2011)

[41] J. Blok and D. G. LeGrand, "Dielectric Breakdown of Polymer Films", J. Appl. Phys. **40**, 288 (1969)

[42] J.A. Stratton, *Electromagnetic Theory*, (International series in pure and applied physics, New York: McGraw-Hill, 1941) chap. 3

[43] D. Ricard, P. Roussignol, and C. Flytzanis, “Surface mediated enhancement of optical phase conjugation in metal colloids”, Opt. Lett. **10**, 511–513 (1985).